Inside Out: Inverse Problems
MSRI Publications
Volume **47**, 2003

Near-Field Tomography

P. SCOTT CARNEY AND JOHN C. SCHOTLAND

Abstract. We consider the inverse scattering problem for wave fields containing evanescent components. Applications to near-field optics and tomographic imaging with subwavelength resolution are described.

Contents

1. Introduction

This article is concerned with a class of inverse problems that arise in near-field optics. These problems may be considered to be special cases of the more general problem of inverse scattering with wave fields containing evanescent components. To place the work described herein in context, we begin with some background information on near-field optical microscopy.

Microscopy is both modern and ancient, beginning nearly four centuries ago with the advent of the Galilean microscope, around 1610. To the extent that Galileo's telescope changed our perspective on the place of humankind in the universe, the microscope changed our perception of the stuff of which we are made. For over 250 years microscopists saw lens design and manufacture as the limiting factors in resolving power. Abbe [1] and Rayleigh [2] separately determined that no matter the physical aparatus, the linear size of the smallest feature that may be resolved with monochromatic, or quasi-monochromatic, light is on the order of the central wavelength of the light. However, the analyses of Abbe and Rayleigh were predicated on the restriction that the imaging instrument is several wavelengths or more from the object. Near-field optical techniques surpass the Abbe–Rayleigh limits by doing away with this restriction.

Near-field optical microscopy has developed dramatically in recent years [3; 4; 5]. The ubiquity of the need for microscopic inspection techniques has brought the intellectual resources of several disparate disciplines to bear on the task of improving the basic methods and putting them to novel application. Conspicuous among those applications are the imaging of biological samples, the inspection and manipulation of nano-electronic components in semiconductor technology, and the inspection and activation of nano-optical devices.

The first proposal of a method to circumvent the Rayleigh resolution limit was put forward by Synge [6] in 1928. Synge proposed that a thin sample be illuminated through a subwavelength aperture. By recording the transmitted light as a function of aperture position, a subwavelength resolved image of the sample may be acquired. Today this method is known as near-field scanning optical microscopy (NSOM) [3; 4; 6; 7; 8; 9; 10; 11] or scanning near-field optical microscopy (SNOM); it is practiced in many variations including the reciprocal arrangement in which the sample is illuminated by a source in the far zone and light is collected through a small aperture. The role of the small aperture is now played by the tip of a tapered optical fiber, a technique not known to Synge. A number of other modalities that fall under the umbrella of near-field optics are subsequently discussed (Figure 1).

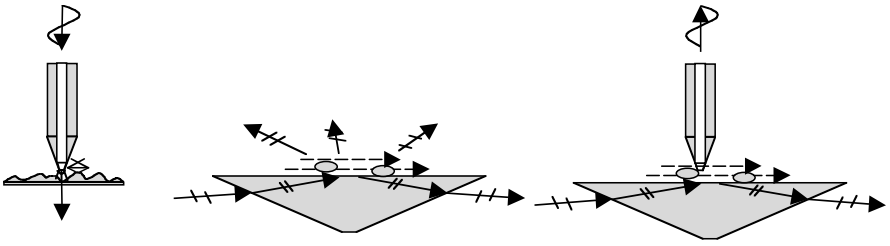

Figure 1. Basic experiments of near-field optics: left, near-field scanning optical microscopy (NSOM); middle, total internal reflection microscopy (TIRM); right, photon scanning tunneling microscopy (PSTM).

Near-field scanning optical microscopy. NSOM has attracted considerable attention as a technique to obtain images of surfaces with subwavelength resolution. This achievement is particularly important for imaging structures where spectroscopic concerns or sample handling requirements dictate the use of lower frequency fields and yet high spatial resolution is still required. Various experimental modalities are in practical use. Two prominent examples are collection mode NSOM and illumination mode NSOM. In illumination mode NSOM, a tapered fiber probe with a sub-wavelength size aperture serves as a source of illumination in the near-zone of the sample. The scattered field intensity is then measured and recorded as a function of the probe position while the probe is scanned over the sample. In collection mode NSOM, the fiber probe serves to detect the total field in the near-zone as the sample is illuminated by a source in the far zone.

There are certain limitations of NSOM as currently practiced. Despite the fact that the sample may present a complicated three-dimensional structure, NSOM produces only a two-dimensional image. Indeed, rather than being an imaging method, it is more accurate to say that NSOM maps the sub-wavelength structure of the optical near-field intensity above the sample. Under certain simplifying assumptions, such as homogeneity of the bulk optical properties of the sample [12; 13; 14; 15], the images produced in these experiments may be related to the sample structure. However, for the more general case in which the topography of the sample and the bulk optical properties both vary, the relationship between the near-field intensity and the sample structure has proven ambiguous [16]. To appreciate this point we consider simulations of the NSOM image of a collection of point scatterers as shown in Figure 2. As is well noted in the literature, the topmost layer of scatterers dominates the conventional (nontomographic) image. When the top layer is removed from the simulation, the conventional image, made with the tip now $\lambda/4$ from the nearest layer, manifests blurring similar to that observed in experiments in which the scanning tip is withdrawn from the sample [10]. See Figure 2.

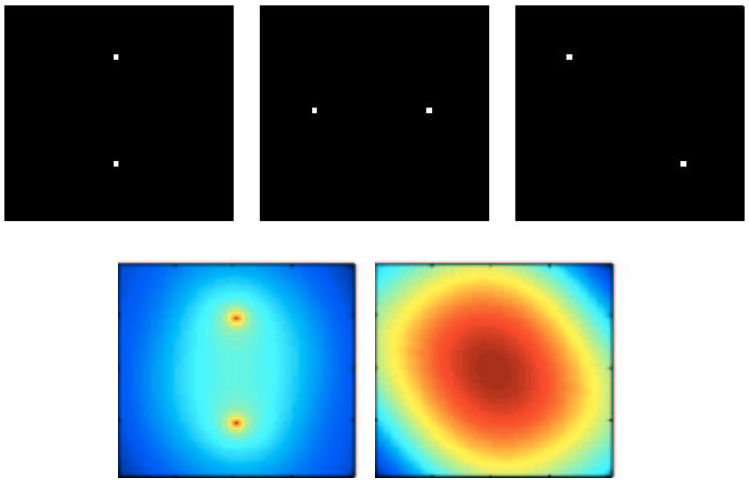

Figure 2. A simulated NSOM image. In each frame the field of view is $\lambda \times \lambda$. The model scatterer consists of six point scatterers distributed in three planes, $z = 0.05\lambda$, $z = 0.25\lambda$, and $z = 0.45\lambda$; the successively deeper planes are shown from left to right in the top row. The figure on the left in the botom row shows the results of a scalar simulation of a collection mode NSOM image made by scanning in the $z = 0$ plane. Illumination is provided by a normally incident plane wave. The figure on the right in the bottom row is the same simulation with the scatterers in the $z = 0.05\lambda$ plane removed.

Total internal reflection microscopy. Essential to the near-field modality of NSOM is the presence of inhomogeneous, or evanescent, modes of the illumination field. Specifically, the illuminating field consists of a superposition of plane waves including the high spatial frequency evanescent plane waves. These waves are super-oscillatory parallel to some reference plane and are exponentially decaying away from the plane. The super-resolving capabilities of NSOM may be attributed to the high spatial frequency of the evanescent waves. Instead of generating these modes at the small aperture in NSOM, they may be generated at the interface of two media by total internal reflection as is done in total internal reflection microscopy (TIRM).

TIRM has been in practical use for decades. This technique has primarily been used as a means of surface inspection [17; 18], though the sensitivity of the field to distance along the decay axis has been used to advantage in applications such as the measurement of distance between two surfaces [19]. Until recently the opportunities for transverse superresolution made possible by the high spatial frequency content of the probe field have been largely over-looked. However, recently a direct imaging approach resulting from the marriage of standing-wave illumination techniques and TIRM has been described [20; 21], achieving transverse resolution of $\lambda/7$.

Photon scanning tunneling microscopy. At the intersection of NSOM and TIRM modalities is the method referred to as photon scanning tunneling microscopy (PSTM) [3; 22; 23]. In this technique the object is illuminated by an evanescent wave generated at the face of a prism or slide (as in TIRM), and the scattered field is detected via a tapered fiber probe in the near-zone of the sample (as in NSOM). Because PSTM is a dark field method, that is the signal is zero if the sample is absent, PSTM generally offers a better signal to noise ratio than NSOM.

Inverse scattering and near-field tomography. In all of the above mentioned modalities, the connection between the measured field and the sample properties has proven to be problematic. Variations in surface height may be indistinguishable from variations in the refractive index of the sample. To clarify the meaning of the measurements and to provide three-dimensional imaging capability, it is desirable to find a solution to the near-field inverse scattering problem.

There is an extensive body of literature on the far-field inverse scattering problem[24]. The inverse scattering problem for near field optics presents challenges and opportunities unlike those encountered in the far-field problem. When, as in the far-field, all waves are homogeneous, the scattering data may be related to a Fourier transform of the sample structure. In contrast, the near-field problem, due to the presence of evanescent fields, will generally involve data related to the object structure through a Fourier–Laplace transform. Because the inversion of the Laplace transform is ill-posed, inverse scattering in the near-field has been thought unfeasible. However, the inverse scattering problem is also over-determined so that it may be observed that there exist many copies of the Fourier–Laplace transform of the object structure encoded on the scattering data. This over-specification of the object structure effectively allows for the averaging of multiple unstable reconstructions to produce a stable reconstruction. The means to accomplish such averaging may be obtained from the analytic construction of the pseudoinverse of the forward scattering operator. Results in this direction have been reported for the TIRM, NSOM and PSTM modalities [25; 26; 27]. The use of inverse scattering methods to reconstruct tomographic images in near-field optics is called near-field tomography.

Near-field power extinction tomography. The preceding discussion focused on inverse scattering methods for extant near-field imaging modalities. It should be stressed that in order to carry-out the program of inverse scattering and object reconstruction described herein, the measurements must be phase sensitive. In certain modalities (NSOM, PSTM), the measurements are intrinsically holographic, producing clear interference between the illuminating field and the scattered field. For other modalities (the TIRM variants) the scattered field must be measured interferometrically with a separate reference field. Because these measurements must be made with multiple directions of illumination, the holographic approach may be somewhat challenging to implement. See Figure 3.

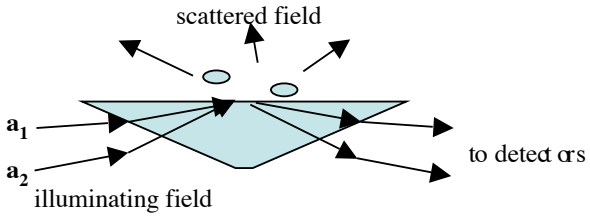

Figure 3. Illustrating the near-field power extinction tomography experiment. Two plane waves are totally internally reflected at the prism face generating evanescent wave. Frustration of the total internal reflection due to the presence of the scatterer generates a scattered field. The power content of the reflected beams is monitored.

To circumvent the phase problem it is desirable to effect reconstruction of the sample structure from measurements only of the power transmitted through the object as is done in X-ray computed tomography. For a scattering sample, a single illuminating wave will not provide sufficient information because the field fails to propagate on a line or even in a rectilinear manner as described by geometrical optics. It was recently shown that knowledge of the three dimensional structure of a scattering medium may be inferred from the power lost by the probe field to scattering and absorption [28; 29] when *two* coherent plane waves illuminate the sample. This result follows, in part, from a generalization of the optical cross-section theorem that applies when more than one wave is incident on the scatterer and allows for the incident waves to be evanescent. Making use of these results, a new modality has recently been proposed in which a sample is illuminated by two superposed evanescent plane waves at the surface of a prism or slab [30]. In the absence of a sample on the prism face, all of the power incident on the interface is reflected. In the presence of the sample, a certain amount of power is coupled into propagating modes and a certain amount of power is absorbed by the object. The total power lost from the incident field due to the presence of the sample is referred to as the extinguished power. The extinguished power carries information about the structure of the scatterer. In order to obtain a complete description of the object, the power content of the internally reflected beams is monitored as the phase between the illuminating waves is varied. Thus a phase measurement problem is traded for a phase control problem, a generally more tractable one. Varying the phase relationship between the two waves causes the interference pattern of the incident field to shift and probe other parts of the object. The higher the spatial frequency of the evanescent waves used to probe the sample, the more rapidly the field falls off as a function of depth into the sample. For this reason the resolution of tomographs generated from these measurements falls off with depth into the sample, as with the other near-field modalities. This method is known as near-field power extinction tomography, or when the probe field is light, near-field optical power extinction tomography.

The remainder of this article is organized as follows. In Section 2 those aspects of scattering theory, for both scalar and electromagnetic waves, that are necessary for the treatment of the forward scattering problem in near-field tomography are discussed. In Section 3 the forward problems for four separate experimental modalities are considered: scanning near-field tomography, total internal reflection tomography, photon scanning tunneling tomography, and near-field power extinction tomography. In each case the integral equations that relate the three-dimensional structure of the sample susceptibility to the scattered field are derived. In Section 4 a unified approach to the inverse problem is developed by construction of the singular value decompostion of the relevant forward scattering operators. Issues of sampling as well as effects due to incomplete and limited data are addressed and the results explored numerically. Finally, in Section 5 a summary of our results and a discussion of future research directions is presented.

2. Scattering Theory

In this section those aspects of scattering theory necessary for the formulation of the forward problem in near-field tomography are reviewed. Scalar waves are discussed first followed by a parallel treatment of the vector theory of electromagnetic scattering. It may be noted that the vector theory is essential for near-field optics since the scalar approximation to the scattering of electromagnetic waves is invalid when the dielectric susceptibility varies on subwavelength scales. Nevertheless, the scalar theory is of independent physical interest since it describes, for example, the scattering of acoustic waves in acoustic microscopy [31; 32; 33].

2A. Scalar Case

Basic equations. Consider an experiment in which an inhomogeneous sample is deposited on a homogeneous substrate. The substrate is assumed to be thick so that only one face need be considered, thus defining an interface between two half-spaces. The index of refraction in the lower half-space $z < 0$ (the substrate) has a constant value n. The index of refraction in the upper half-space $z \geq 0$ varies within the domain of the sample but otherwise has a value of unity. The sample is illuminated either from above (reflection geometry) or below (transmission geometry) by a monochromatic scalar wave of frequency $\omega = ck_0$. The scalar field $U(\boldsymbol{r})$ obeys the reduced wave equation

$$\nabla^2 U(\boldsymbol{r}) + k_0^2\big(n^2(z) + 4\pi\eta(\boldsymbol{r})\big)U(\boldsymbol{r}) = -4\pi S(\boldsymbol{r}),$$

where $\eta(\boldsymbol{r})$ is the susceptibility of the sample, k_0 is the free-space wavenumber, $n(z)$ is the z-dependent index of refraction as described above, and $S(\boldsymbol{r})$ is the source density. The total field consists of two parts:

$$U(\boldsymbol{r}) = U_i(\boldsymbol{r}) + U_s(\boldsymbol{r}),$$

where $U_i(\boldsymbol{r})$ and $U_s(\boldsymbol{r})$ are the incident and scattered fields, respectively. The incident field may be identified as the field that would exist in the absence of the sample. U_i obeys the reduced wave equation

$$\nabla^2 U_i(\boldsymbol{r}) + k_0^2 n^2(z) U_i(\boldsymbol{r}) = -4\pi S(\boldsymbol{r}). \tag{2–1}$$

It follows that the scattered field satisfies the equation

$$\nabla^2 U_s(\boldsymbol{r}) + k_0^2 n^2(z) U_s(\boldsymbol{r}) = -4\pi k_0^2 \eta(\boldsymbol{r}) U(\boldsymbol{r}).$$

Integral equations. The analysis will be facilitated by use of the Green's function, $G(\boldsymbol{r}, \boldsymbol{r}')$ which obeys the equation

$$\nabla^2 G(\boldsymbol{r}, \boldsymbol{r}') + n^2(z) k_0^2 G(\boldsymbol{r}, \boldsymbol{r}') = -4\pi\delta(\boldsymbol{r} - \boldsymbol{r}')$$

and satisfies the boundary conditions

$$\begin{aligned} G(\boldsymbol{r}, \boldsymbol{r}')\big|_{z=0^+} &= G(\boldsymbol{r}, \boldsymbol{r}')\big|_{z=0^-}, \\ \hat{\boldsymbol{z}} \cdot \nabla G(\boldsymbol{r}, \boldsymbol{r}')\big|_{z=0^+} &= \hat{\boldsymbol{z}} \cdot \nabla G(\boldsymbol{r}, \boldsymbol{r}')\big|_{z=0^-} \end{aligned}$$

on the $z = 0$ plane. Following standard procedures it may then be seen that the incident field is given by

$$U_i(\boldsymbol{r}) = \int d^3 r' G(\boldsymbol{r}, \boldsymbol{r}') S(\boldsymbol{r}').$$

The scattered field obeys the integral equation

$$U_s(\boldsymbol{r}) = k_0^2 \int d^3 r'\, G(\boldsymbol{r}, \boldsymbol{r}') U(\boldsymbol{r}') \eta(\boldsymbol{r}'). \tag{2–2}$$

The Green's function $G(\boldsymbol{r}, \boldsymbol{r}')$ may be expressed in the plane-wave decomposition [34; 35]

$$G(\boldsymbol{r}, \boldsymbol{r}') = \int \frac{d^2 q}{(2\pi)^2} g(z, z'; \boldsymbol{q}) \exp\bigl(i\boldsymbol{q} \cdot (\boldsymbol{\rho} - \boldsymbol{\rho}')\bigr). \tag{2–3}$$

Explicit expressions for $g(z, z'; \boldsymbol{q})$ in the half-space geometry are given in the Appendix. In free space it can be shown that

$$g(z, z'; \boldsymbol{q}) = \frac{2\pi i}{k_z(\boldsymbol{q})} \exp\bigl(i k_z(\boldsymbol{q}) \, |z - z'|\bigr).$$

The notation should be understood to mean that $\boldsymbol{r} = (\boldsymbol{\rho}, z)$ and

$$k_z(\boldsymbol{q}) = \sqrt{k_0^2 - q^2}.$$

The plane wave modes appearing in (2–3) are labeled by the transverse part of the wave vector $\boldsymbol{q}$. The modes for which $|\boldsymbol{q}| \leq k_0$ correspond to propagating waves while the modes with $|\boldsymbol{q}| > k_0$ correspond to evanescent waves. For these modes $k_z(\boldsymbol{q})$ is pure imaginary. This leads to exponential decay of the field with propagation and a corresponding loss of high spatial frequency components.

The integral equation (2–2) has the form of the Lippmann–Schwinger equation of quantum scattering theory. It provides a complete description of the scattering of the incident wave within the sample and the substrate. If the scattered wave is much weaker than the incident field, then we may replace the field by the incident field in the right hand side of (2–2). Equation (2–2) thus becomes

$$U_s(\boldsymbol{r}) = \int d^3r' G(\boldsymbol{r}, \boldsymbol{r}') U_i(\boldsymbol{r}') \eta(\boldsymbol{r}'). \tag{2–4}$$

This result, which is referred to as the first Born approximation for the scattered field, is valid for small, weakly scattering objects.

The optical theorem. Energy conservation leads to a fundamental result in scattering theory known as the optical theorem. In its most general form [36], it expresses the total power P extinguished from the incident field as the integral

$$P = 4\pi k_0 \operatorname{Im} \int d^3r U_i^*(\boldsymbol{r}) U(\boldsymbol{r}) \eta(\boldsymbol{r}). \tag{2–5}$$

The depletion of the power from the incident beam may be seen to arise from the interference between the total field and the incident field within the region of the scatterer.

The result is better known for a restricted case. If the incident field consists of a homogeneous, or propagating, plane wave with amplitude a and wave vector $\boldsymbol{k}$,

$$U_i(\boldsymbol{r}) = a e^{i\boldsymbol{k}\cdot\boldsymbol{r}},$$

then P is related to the scattering amplitude in the forward (incident) direction by the expression

$$P = |a|^2 \frac{4\pi}{k_0} \operatorname{Im} A(\boldsymbol{k}, \boldsymbol{k}). \tag{2–6}$$

Here $A(\boldsymbol{k}, \boldsymbol{k}')$ is the scattering amplitude associated with the transition *via* scattering of a plane wave with wave vector $\boldsymbol{k}$ to a plane wave with wave vector $\boldsymbol{k}'$. It is defined by

$$A(\boldsymbol{k}, \boldsymbol{k}') = k_0^2 a^{-1} \int d^3r e^{-i\boldsymbol{k}'\cdot\boldsymbol{r}} U(\boldsymbol{r}) \eta(\boldsymbol{r}). \tag{2–7}$$

Equation (2–6) is the classical form of the optical theorem known in quantum scattering theory [37; 38; 39].

2B. Vector Case. To adequately describe the physics of near-field optical microscopy, the vector theory of electromagnetic scattering must be invoked. The starting point for such an investigation is the set of Maxwell's equations. It will be assumed that the material of the sample is linear and nonmagnetic (a broad class of materials). As in the scalar case, the problem is set in a half-space with the upper ($z \geq 0$) half-space being the vacuum plus the sample and the lower ($z < 0$) half-space being filled with a material of refractive index n.

Basic equations. The fields are entirely descibed by specifying the electric field everywhere. The magnetic field thus may be ignored as redundant and it is sufficient to consider only the electric field $\boldsymbol{E}$. For a monochromatic source, $\boldsymbol{E}$ satisfies the reduced wave equation

$$\nabla \times \nabla \times \boldsymbol{E}(\boldsymbol{r}) - k_0^2(n^2(z) + 4\pi\eta(\boldsymbol{r}))\boldsymbol{E}(\boldsymbol{r}) = 4\pi k_0^2 \boldsymbol{P}(\boldsymbol{r}).$$

Here the dielectric suspectibilty $\eta(\boldsymbol{r})$ is related to the permittivity $\varepsilon(\boldsymbol{r})$ by $\varepsilon(\boldsymbol{r}) = n^2(z) + 4\pi\eta(\boldsymbol{r})$, and $\boldsymbol{P}(\boldsymbol{r})$ is the dielectric polarization (which acts as a source of the electric field). Again the field consists of two parts,

$$\boldsymbol{E}(\boldsymbol{r}) = \boldsymbol{E}^i(\boldsymbol{r}) + \boldsymbol{E}^s(\boldsymbol{r}). \tag{2–8}$$

The incident field $\boldsymbol{E}^i(\boldsymbol{r})$ obeys the equation

$$\nabla \times \nabla \times \boldsymbol{E}^i(\boldsymbol{r}) - k_0^2 n^2(z)\boldsymbol{E}^i(\boldsymbol{r}) = 4\pi k_0^2 \boldsymbol{P}(\boldsymbol{r}).$$

Thus the scattered field $\boldsymbol{E}^s(\boldsymbol{r})$ satisfies

$$\nabla \times \nabla \times \boldsymbol{E}^s(\boldsymbol{r}) - k_0^2 n^2(z)\boldsymbol{E}^s(\boldsymbol{r}) = 4\pi k_0^2 \eta(\boldsymbol{r})\boldsymbol{E}(\boldsymbol{r}).$$

Integral equations. The fields may be expressed in integral equation form by use of the Green's tensor $\boldsymbol{G}(\boldsymbol{r}, \boldsymbol{r}')$ which satisfies

$$\nabla \times \nabla \times \boldsymbol{G}(\boldsymbol{r}, \boldsymbol{r}') - k_0^2 n^2(z)\boldsymbol{G}(\boldsymbol{r}, \boldsymbol{r}') = 4\pi\delta(\boldsymbol{r} - \boldsymbol{r}')\boldsymbol{I}$$

where $\boldsymbol{I}$ is the unit tensor. The Green's tensor must also obey the boundary conditions

$$\begin{aligned} \hat{\boldsymbol{z}} \times \boldsymbol{G}(\boldsymbol{r}, \boldsymbol{r}')\big|_{z=0^+} &= \hat{\boldsymbol{z}} \times \boldsymbol{G}(\boldsymbol{r}, \boldsymbol{r}')\big|_{z=0^-}, \\ \hat{\boldsymbol{z}} \times \nabla \times \boldsymbol{G}(\boldsymbol{r}, \boldsymbol{r}')\big|_{z=0^+} &= \hat{\boldsymbol{z}} \times \nabla \times \boldsymbol{G}(r, \boldsymbol{r}')\big|_{z=0^-} \end{aligned}$$

on the $z = 0$ plane. For later reference we note the plane-wave decomposition of $G_{\alpha\beta}(\boldsymbol{r}, \boldsymbol{r}')$ [40] :

$$G_{\alpha\beta}(\boldsymbol{r}, \boldsymbol{r}') = \int \frac{d^2q}{(2\pi)^2} g_{\alpha\beta}(\boldsymbol{q}, z) \exp\big(i\boldsymbol{q} \cdot (\boldsymbol{\rho} - \boldsymbol{\rho}')\big). \tag{2–9}$$

Explicit expressions for $g_{\alpha\beta}(\boldsymbol{q}, z)$ in the half-space geometry are given in the Appendix. In free space it can be shown that

$$g_{\alpha\beta}(z, z'; \boldsymbol{q}) = \frac{2\pi i}{k_z(\boldsymbol{q})}\big(\delta_{\alpha\beta} - k_0^{-2} k_\alpha(\boldsymbol{q}) k_\beta(\boldsymbol{q})\big) \exp\big(ik_z(\boldsymbol{q})|z - z'|\big),$$

where $\boldsymbol{k}(q) = (\boldsymbol{q}, k_z(\boldsymbol{q}))$. Using these results, it may be seen that the incident field is given by

$$E^i_\alpha(\boldsymbol{r}) = k_0^2 \int d^3r' G_{\alpha\beta}(\boldsymbol{r}, \boldsymbol{r}') P_\beta(\boldsymbol{r}'), \tag{2–10}$$

where the summation convention over repeated indices applies. The scattered field obeys the integral equation

$$E^s_\alpha(\boldsymbol{r}) = k_0^2 \int d^3r' G_{\alpha\beta}(\boldsymbol{r}, \boldsymbol{r}') E_\beta(\boldsymbol{r}')\eta(\boldsymbol{r}').$$

Within the accuracy of the first Born approximation, the electric field may be replaced by the incident field in the right hand side of the above equation thus obtaining

$$E^s_\alpha(\boldsymbol{r}) = k_0^2 \int d^3r' G_{\alpha\beta}(\boldsymbol{r},\boldsymbol{r}') E^i_\beta(\boldsymbol{r}')\eta(\boldsymbol{r}'). \tag{2–11}$$

The optical theorem. Energy conservation for Maxwell's equations leads to the optical theorem for electromagnetic waves. The extinguished power may be shown to be given by the expression [36]

$$P = \frac{1}{2} ck_0 \operatorname{Im} \int d^3r \boldsymbol{E}^{i\,*}(\boldsymbol{r}) \cdot \boldsymbol{E}(\boldsymbol{r})\eta(\boldsymbol{r}). \tag{2–12}$$

If the incident field is a propagating plane wave with amplitude $\boldsymbol{a}$ and wave vector $\boldsymbol{k}$

$$\boldsymbol{E}^i(\boldsymbol{r}) = \boldsymbol{a} e^{i\boldsymbol{k}\cdot\boldsymbol{r}},$$

then P is related to the scattering amplitude by

$$P = |\boldsymbol{a}|^2 \frac{4\pi}{k_0} \operatorname{Im}\big(\boldsymbol{A}(\boldsymbol{k},\boldsymbol{k}) \cdot \hat{\boldsymbol{e}}^*\big),$$

where $\hat{\boldsymbol{e}}$ is a unit vector in the $\boldsymbol{a}$ direction. Here $\boldsymbol{A}(\boldsymbol{k},\boldsymbol{k}')$ is the vector scattering amplitude defined by

$$\boldsymbol{A}(\boldsymbol{k},\boldsymbol{k}') = \frac{k_0^2 c}{8\pi|\boldsymbol{a}|} \int d^3r e^{-i\boldsymbol{k}'\cdot\boldsymbol{r}} \boldsymbol{E}(\boldsymbol{r})\eta(\boldsymbol{r}).$$

3. Forward Problem

The forward problem in near-field tomography is the problem of computing the scattered field from the susceptibility. Analyses are carried out here separately for each experimental modality, making use of the scalar and vector scattering theory developed in Section 2. A common form relating the susceptibility to the scattering data will emerge.

3A. Scanning Near-Field Tomography. Scanning near-field tomography is based on the scanning modalities of near-field optics, namely NSOM. The two principal genres of NSOM are illumination mode and collection mode. The nomenclature reflects the role of the probe in each modality. In collection mode NSOM, a sharp, tapered optical fiber tip is coated with metal and a small aperture is exposed at the end of the fiber probe. The sample is illuminated by a source located in the far-zone of the sample and the total field is collected in the near-zone of the sample through the small aperture in the probe as the probe is scanned over the sample. In illumination mode NSOM, a probe, like that used in collection mode, is scanned over the sample in the near-zone. However, the source of illumination is light transmitted through the fiber and the small aperture at the tip. The field scattered by the sample is then collected and measured in the far-zone and recorded as a function of probe position.

To effect tomographic reconstruction of the sample it is necessary to perform all measurements with phase sensitivity. In the case of collection mode NSOM, the scattered field is naturally in superposition with the incident field and so the measurements are intrinsically holographic [42; 5]—a situation analogous to the Gabor hologram[43; 44; 45]. Illumination mode, however, is not intrinsically holographic and so the phase of the scattered field must be ascertained by some other means, possibly by interference with some reference field coherent with the illuminating field [46] as is done in the far field problem to produce the Leith–Upatnieks hologram [43; 47; 48]. In this article, it will be assumed that the scattered field is measured with phase sensitivity and we will not dwell on the experimental particulars, though it should be noted that the problem is nontrivial.

3A1. Scalar case

Illumination mode. An illustration of illumination mode NSOM is shown in Figure 4. It is assumed that the sample lies on a substrate which is defined by the plane $z = 0$ and is illuminated with a point source which lies in the plane $z = z_s$. The sample lies in the region $0 \leq z \leq z_s$ and is described by a susceptibility $\eta(\boldsymbol{r})$. If the point source has unit amplitude and is located at the position $\boldsymbol{r}_1 = (\boldsymbol{\rho}_1, z_s)$ then, according to (2–1) and (2–2), $S(\boldsymbol{r}) = \delta(\boldsymbol{r} - \boldsymbol{r}_1)$ and hence $U_i(\boldsymbol{r}) = G(\boldsymbol{r}, \boldsymbol{r}_1)$. The scattered field is then given by

$$U_s(\boldsymbol{r}) = k_0^2 \int d^3r' G(\boldsymbol{r}, \boldsymbol{r}') G(\boldsymbol{r}', \boldsymbol{r}_1) \eta(\boldsymbol{r}').$$

Suppose that the observation point $\boldsymbol{r}$ is in the far field of the sample and that the field is measured in the $z > 0$ half-space. This situation is referred to as the reflection geometry; the transmission geometry, in which the field is measured in the $z < 0$ half-space, will not be considered here but is amenable to a similar treatment. It may be seen that for $|\boldsymbol{r}| \gg |\boldsymbol{r}'|$ the leading term in the asymptotic expansion of the Green's function is given by

$$G(\boldsymbol{r}, \boldsymbol{r}') \sim \frac{e^{ik_0 r}}{r} e^{-i\boldsymbol{k}(\boldsymbol{q})\cdot\boldsymbol{r}'} \big(1 + R(\boldsymbol{q}) e^{2ik_z(\boldsymbol{q})z'}\big), \tag{3–1}$$

where $\boldsymbol{k}(\boldsymbol{q})$ lies in the direction of $\boldsymbol{r}$, $|\boldsymbol{q}| \leq k_0$ and $R(\boldsymbol{q})$ is the reflection coefficient defined in the Appendix. The scattered field behaves as an outgoing spherical wave. It may be expressed in terms of the scattering amplitude $A(\boldsymbol{\rho}_1, \boldsymbol{q})$ which depends on the position of the source and the propagation vector $\boldsymbol{k}(\boldsymbol{q})$ in the direction of observation:

$$U_s(\boldsymbol{r}) \sim \frac{e^{ik_0 r}}{r} A(\boldsymbol{\rho}_1, \boldsymbol{q}),$$

where

$$A(\boldsymbol{\rho}_1, \boldsymbol{q}) = k_0^2 \int d^3r e^{-i\boldsymbol{k}(\boldsymbol{q})\cdot\boldsymbol{r}} \big(1 + R(\boldsymbol{q}) e^{2ik_z(\boldsymbol{q})z}\big) G(\boldsymbol{r}, \boldsymbol{r}_1) \eta(\boldsymbol{r}). \tag{3–2}$$

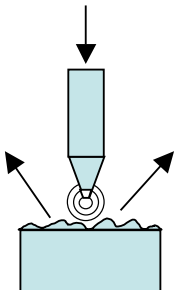

Figure 4. Illumination mode geometry. The sample is illuminated by light from the probe tip in the near-zone. The scattered field is measured in the far zone and recorded as a function of tip position.

We assume that the source is scanned over a square lattice with lattice spacing h, thus sampling the scattering amplitude. It will prove useful to define a data function $\Phi(\boldsymbol{q}_1, \boldsymbol{q}_2)$ by the lattice Fourier transform

$$\Phi(\boldsymbol{q}_1, \boldsymbol{q}_2) = \sum_{\boldsymbol{\rho}_1} e^{i\boldsymbol{q}_1 \cdot \boldsymbol{\rho}_1} A(\boldsymbol{\rho}_1, \boldsymbol{q}_2),$$

where the sum over $\boldsymbol{\rho}_1$ is carried out over all lattice vectors and $\boldsymbol{q}_1$ belongs to the first Brillouin zone (FBZ) of the lattice. In this case FBZ$=[-\pi/h, \pi/h] \times [-\pi/h, \pi/h]$. It may be observed that if $\boldsymbol{q}_1$ is not limited to the FBZ, the data outside the FBZ are redundant. Making use of (2–3), (3–2) and the identity

$$\sum_{\boldsymbol{\rho}} e^{i\boldsymbol{q} \cdot \boldsymbol{\rho}} = \left(\frac{2\pi}{h}\right)^2 \sum_{\boldsymbol{q}'} \delta(\boldsymbol{q} - \boldsymbol{q}'),$$

where $\boldsymbol{q}'$ denotes a reciprocal lattice vector [1], we find that

$$\Phi(\boldsymbol{q}_1, \boldsymbol{q}_2) = \left(\frac{k_0}{h}\right)^2 \int d^3 r \sum_{\boldsymbol{q}} \exp\big(i(\boldsymbol{q}_1 - \boldsymbol{q}_2 - \boldsymbol{q}) \cdot \boldsymbol{\rho}\big)\big(1 + R(\boldsymbol{q}_2) e^{2ik_z(\boldsymbol{q}_2) z}\big)$$
$$\times e^{ik_z(\boldsymbol{q}_2) z} g(z, z_s; \boldsymbol{q}_1 - \boldsymbol{q}) \eta(\boldsymbol{r}). \quad (3\text{–}3)$$

It is natural to reconstruct $\eta(\boldsymbol{r})$ on the same lattice that field is sampled. In that case the inverse problem will prove more tractable if $\eta(\boldsymbol{r})$ is assumed to be band limited so as to be consistent with the lattice on which $A(\boldsymbol{\rho}_1, \boldsymbol{q}_2)$ is sampled. Then the sum over $\boldsymbol{q}$ may be truncated and only the $\boldsymbol{q} = 0$ term contributes to $\Phi(\boldsymbol{q}_1, \boldsymbol{q}_2)$. Thus (3–3) may be written in the form of the integral equation

$$\Phi(\boldsymbol{q}_1, \boldsymbol{q}_2) = \int d^3 r K(\boldsymbol{q}_1, \boldsymbol{q}_2; \boldsymbol{r}) \eta(\boldsymbol{r}). \quad (3\text{–}4)$$

Here the kernel

$$K(\boldsymbol{q}_1, \boldsymbol{q}_2; \boldsymbol{r}) = e^{i(\boldsymbol{q}_1 - \boldsymbol{q}_2) \cdot \boldsymbol{\rho}} \kappa(\boldsymbol{q}_1, \boldsymbol{q}_2; z),$$

[1] The reciprocal lattice consists of all points in the plane of the form $(2n\pi/h, 2m\pi/h)$ with n, m being integers.

where

$$\kappa(\boldsymbol{q}_1, \boldsymbol{q}_2; z) = \left(\frac{k_0}{h}\right)^2 \left(1 + R(\boldsymbol{q}_2) e^{2ik_z(\boldsymbol{q}_2)z}\right) e^{ik_z(\boldsymbol{q}_2)z} g(z, z_s; \boldsymbol{q}_1).$$

Equation (3–4) expresses the forward problem in scalar illumination mode scanning near-field tomography.

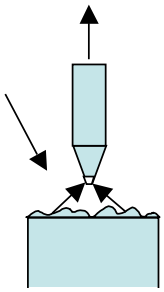

Figure 5. Collection mode geometry. The sample is illuminated from the far zone. The field is collected at the probe tip and recorded as a function of tip position.

Collection mode. An illustration of collection mode NSOM in the reflection geometry is shown in Figure 5. In this situation the sample is illuminated from the far zone by an incident plane wave and the scattered field is detected in the near-zone by means of an idealized point detector. Evidently, the incident wave may be reflected from the boundary and is of the form

$$U_i(\boldsymbol{r}) = \left(1 + R(\boldsymbol{q}) e^{2ik_z(\boldsymbol{q})z}\right) e^{i\boldsymbol{k}_i(\boldsymbol{q})\cdot\boldsymbol{r}},$$

where $\boldsymbol{k}_i(\boldsymbol{q}) = (\boldsymbol{q}, -k_z(\boldsymbol{q}))$, $R(\boldsymbol{q})$ is the reflection coefficient (defined in the Appendix), and it has been assumed that the incident wave is of unit amplitude. The scattered field, measured in the $z = z_d$ plane at a point with coordinate $\boldsymbol{r} = (\boldsymbol{\rho}, z_d)$, is given by the expression

$$U_s(\boldsymbol{r}) = k_0^2 \int d^3r' \left(1 + R(\boldsymbol{q}) e^{2ik_z(\boldsymbol{q})z'}\right) e^{i\boldsymbol{k}_i(\boldsymbol{q})\cdot\boldsymbol{r}'} G(\boldsymbol{r}, \boldsymbol{r}') \eta(\boldsymbol{r}'),$$

which follows from (2–4).

The scattered field is sampled on a square lattice with lattice spacing h and, as in the case of illumination mode, the data function is defined by the lattice Fourier transform

$$\Phi(\boldsymbol{q}_1, \boldsymbol{q}_2) = \sum_{\boldsymbol{\rho}} e^{-i\boldsymbol{q}_2\cdot\boldsymbol{\rho}} U_s(\boldsymbol{\rho}, z_d; \boldsymbol{q}_1),$$

where $\boldsymbol{q}_2 \in$ FBZ and the dependence of the scattered field on the transverse component $\boldsymbol{q}_1$ of the incident wave vector has been made explicit. Using the

plane wave decomposition of the Green's function (2–3) and carying out the Fourier transform, we find that

$$\Phi(\boldsymbol{q}_1,\boldsymbol{q}_2)=\Big(\frac{k_0}{h}\Big)^2\int d^3r\sum_{\boldsymbol{q}}\exp\big(i(\boldsymbol{q}_1-\boldsymbol{q}_2-\boldsymbol{q})\cdot\boldsymbol{\rho}\big)$$
$$\times\big(1+R(\boldsymbol{q}_1)e^{2ik_z(\boldsymbol{q}_1)z}\big)e^{-ik_z(\boldsymbol{q}_1)z}g(z_d,z;\boldsymbol{q}_2-\boldsymbol{q})\eta(\boldsymbol{r}).\quad(3\text{–}5)$$

As discussed earlier, $\eta(\boldsymbol{r})$ is assumed to be transversely band limited with a band limit commensurate with the lattice structure. Then (3–5) may be written in the form of the integral equation (3–4) with

$$\kappa(\boldsymbol{q}_1,\boldsymbol{q}_2;z)=\Big(\frac{k_0}{h}\Big)^2\big(1+R(\boldsymbol{q}_1)e^{2ik_z(\boldsymbol{q}_1)z}\big)e^{-ik_z(\boldsymbol{q}_1)z}g(z_d,z;\boldsymbol{q}_2).$$

3A2. Vector case. The mathematical treatment of the vector forward problem for scanning near-field tomography follows closely the scalar case.

Illumination mode. In illumination mode the sample is illuminated by a point source with position $\boldsymbol{r}_1=(\boldsymbol{\rho}_1,z_s)$ which is scanned in the $z=z_s$ plane. The incident field is obtained from (2–10) with the dielectric polarization $\boldsymbol{P}(\boldsymbol{r})=\boldsymbol{p}\delta(\boldsymbol{r}-\boldsymbol{r}_1)$, $\boldsymbol{p}$ being the dipole moment of the source of the field. Thus

$$E^i_\alpha(\boldsymbol{r})=k_0^2G_{\alpha\beta}(\boldsymbol{r},\boldsymbol{r}_1)p_\beta.$$

Using (2–11) the scattered field is seen to be given by

$$E^s_\alpha(\boldsymbol{r})=k_0^4\int d^3r'G_{\alpha\beta}(\boldsymbol{r},\boldsymbol{r}')G_{\beta\gamma}(\boldsymbol{r}',\boldsymbol{r}_1)p_\gamma\eta(\boldsymbol{r}').$$

In the upper half space, for $|\boldsymbol{r}|\gg|\boldsymbol{r}'|$, the Green's tensor assumes the asymptotic form

$$G_{\alpha\beta}(\boldsymbol{r},\boldsymbol{r}')\sim S^{-1}_{\alpha\gamma}(\boldsymbol{q})\tilde g_{\gamma\delta}(\boldsymbol{q},z)S_{\delta\beta}(\boldsymbol{q})\frac{\exp(ik_0r)}{r}\exp\big(-i\boldsymbol{k}(\boldsymbol{q})\cdot\boldsymbol{r}'\big),\qquad(3\text{–}6)$$

where $\boldsymbol{k}(\boldsymbol{q})$ lies in the direction of $\boldsymbol{r}$ and the prefactors are defined in the Appendix. Thus the scattered field in the far-zone in the upper half space takes the form

$$E^s_\alpha(\boldsymbol{r})\sim\frac{e^{ik_0r}}{r}A_\alpha(\boldsymbol{\rho}_1,\boldsymbol{q}).$$

Here the scattering amplitude is given by

$$A_\alpha(\boldsymbol{\rho}_1,\boldsymbol{q})=k_0^2\int d^3re^{-i\boldsymbol{k}(\boldsymbol{q})\cdot\boldsymbol{r}}w_{\alpha\beta}(\boldsymbol{q},z)G_{\beta\gamma}(\boldsymbol{r},\boldsymbol{r}_1)p_\gamma\eta(\boldsymbol{r}),$$

where

$$w_{\alpha\beta}(\boldsymbol{q},z)=k_0^2S^{-1}_{\alpha\gamma}(\boldsymbol{q})\tilde g_{\gamma\delta}(\boldsymbol{q},z)S_{\delta\beta}(\boldsymbol{q}).\qquad(3\text{–}7)$$

As before, a data function is defined through a lattice Fourier transform of the sampled scattering amplitude

$$\Phi_\alpha(\boldsymbol{q}_1,\boldsymbol{q}_2)=\sum_{\boldsymbol{\rho}_1}e^{i\boldsymbol{q}_1\cdot\boldsymbol{\rho}_1}A_\alpha(\boldsymbol{\rho}_1,\boldsymbol{q}_2),$$

where $\boldsymbol{q}_1 \in \mathrm{FBZ}$. Making use of the plane wave decomposition (2–9), it is found that

$$\Phi_\alpha(\boldsymbol{q}_1, \boldsymbol{q}_2) = \left(\frac{k_0}{h}\right)^2 \int d^3r \sum_{\boldsymbol{q}} \exp\bigl(i(\boldsymbol{q}_1 - \boldsymbol{q}_2 - \boldsymbol{q}) \cdot \boldsymbol{\rho}\bigr) \times e^{ik_z(\boldsymbol{q}_2)z} w_{\alpha\beta}(\boldsymbol{q}_2, z) g_{\beta\gamma}(z, z_s; \boldsymbol{q}_1 - \boldsymbol{q}) p_\gamma \eta(\boldsymbol{r}). \quad (3\text{–}8)$$

If $\eta(\boldsymbol{r})$ is transversely band limited, as in the previous cases, with a band limit commensurate with the lattice structure then we find that (3–8) may be written in the form of the integral equation

$$\Phi_\alpha(\boldsymbol{q}_1, \boldsymbol{q}_2) = \int d^3r K_\alpha(\boldsymbol{q}_1, \boldsymbol{q}_2; \boldsymbol{r}) \eta(\boldsymbol{r}). \quad (3\text{–}9)$$

Here the kernel

$$K_\alpha(\boldsymbol{q}_1, \boldsymbol{q}_2; \boldsymbol{r}) = \exp\bigl(i(\boldsymbol{q}_1 - \boldsymbol{q}_2) \cdot \boldsymbol{\rho}\bigr) \kappa_\alpha(\boldsymbol{q}_1, \boldsymbol{q}_2; z),$$

where

$$\kappa_\alpha(\boldsymbol{q}_1, \boldsymbol{q}_2; z) = \left(\frac{k_0}{h}\right)^2 e^{ik_z(\boldsymbol{q}_2)z} w_{\alpha\beta}(\boldsymbol{q}_2, z) g_{\beta\gamma}(z, z_s; \boldsymbol{q}_1) p_\gamma.$$

Equation (3–9) expresses the forward problem for vector illumination mode scanning near-field tomography.

Collection mode. As in the scalar case, collection mode NSOM in the reflection geometry involves illumination of the sample by a source in the far-zone and collection of the near-zone scattered field in the upper half-space. The incident field will be taken to linearly polarized,

$$E^i_\alpha(\boldsymbol{r}) = E^{(0)}_\alpha \bigl(1 + R(\boldsymbol{q}) e^{2ik_z(\boldsymbol{q})z}\bigr) e^{i\boldsymbol{k}_i(\boldsymbol{q}) \cdot \boldsymbol{r}},$$

where $E^{(0)}_\alpha$ is the polarization of the incident field, $R(\boldsymbol{q})$ is the appropriate Fresnel reflection coefficient for the electric field and $\boldsymbol{k}_i(\boldsymbol{q}) = (\boldsymbol{q}, -k_z(\boldsymbol{q}))$. For simplicity, we will consider the incident field to have TE polarization, that is the polarization vector of the incident fields is parallel to the boundary of the half-space. More general states of polarization may also be considered and it is important to note that the signal in NSOM has a strong polarization dependence [16]. Using (2–11), we find that the scattered field, measured in the plane $z = z_d$ is given by the expression

$$E^s_\alpha(\boldsymbol{r}) = k_0^2 \int d^3r' \bigl(1 + R(\boldsymbol{q}) e^{2ik_z(\boldsymbol{q})z'}\bigr) e^{i\boldsymbol{k}_i(\boldsymbol{q}) \cdot \boldsymbol{r}'} G_{\alpha\beta}(\boldsymbol{r}, \boldsymbol{r}') E^{(0)}_\beta \eta(\boldsymbol{r}').$$

The data function is defined as the lattice Fourier transform

$$\Phi_\alpha(\boldsymbol{q}_1, \boldsymbol{q}_2) = \sum_{\boldsymbol{\rho}} e^{-i\boldsymbol{q}_2 \cdot \boldsymbol{\rho}} E^s_\alpha(\boldsymbol{\rho}, z_d; \boldsymbol{q}_1), \quad (3\text{–}10)$$

where $\boldsymbol{q}_2 \in$ FBZ. The plane wave decomposition (2–9) may be utilized to obtain

$$\Phi_\alpha(\boldsymbol{q}_1,\boldsymbol{q}_2) = \left(\frac{k_0}{h}\right)^2 \int d^3r \sum_{\boldsymbol{q}} \exp\bigl(i(\boldsymbol{q}_1-\boldsymbol{q}_2-\boldsymbol{q})\cdot\boldsymbol{\rho}\bigr)\bigl(1+R(\boldsymbol{q}_1)e^{2ik_z(\boldsymbol{q}_1)z}\bigr) \times e^{-ik_z(\boldsymbol{q}_1)z} g_{\alpha\beta}(z_d,z;\boldsymbol{q}_2-\boldsymbol{q}) E_\beta^{(0)}\eta(\boldsymbol{r}). \quad (3\text{–}11)$$

If $\eta(\boldsymbol{r})$ is transversely band limited with a band limit consistent with the lattice structure, then we find that (3–11) may be written in the form of the integral equation (3–9) with

$$\kappa_\alpha(\boldsymbol{q}_1,\boldsymbol{q}_2;z) = \left(\frac{k_0}{h}\right)^2 \bigl(1+R(\boldsymbol{q}_1)e^{2ik_z(\boldsymbol{q}_1)z}\bigr) e^{-ik_z(\boldsymbol{q}_1)z} g_{\alpha\beta}(z_d,z;\boldsymbol{q}_2) E_\beta^{(0)}.$$

3B. Total Internal Reflection Tomography. In total internal reflection tomography, the sample is illuminated by an evanescent wave that is generated by total internal reflection. The scattered field is then measured in the far zone of the scatterer as the direction of the incident wave is varied. See Figure 1. It should be noted that the scattered field must be measured with phase sensitivity.

3B1. Scalar case. The sample resides in vacuum in the geometry described earlier. The sample is illluminated by an evanescent plane wave which is generated by total internal reflection in the half-space with $n > 1$. The field incident on the sample is of the form

$$U_i(\boldsymbol{r}) = e^{i\boldsymbol{k}_1(\boldsymbol{q}_1)\cdot\boldsymbol{r}}, \quad (3\text{–}12)$$

where $\boldsymbol{k}_1(\boldsymbol{q}_1) = (\boldsymbol{q}_1, k_z(\boldsymbol{q}_1))$ is the incident wave vector. The transverse wave vector $\boldsymbol{q}$ satisfies $k_0 \le |\boldsymbol{q}_1| \le nk_0$, where n the index of refraction of the lower half space. Note that k_z is imaginary with the choice of sign dictated by the physical requirement that the field decay exponentially with increasing values of z. In the far zone, the scattered field behaves as an outgoing spherical wave determined by the wave vector $\boldsymbol{k}_2(\boldsymbol{q}_2) = (\boldsymbol{q}_2, k_z(\boldsymbol{q}_2))$ with $|\boldsymbol{q}_2| \le k_0$. Making use of the integral equation (2–4) and the asymptotic form of the outgoing Green's function (3–1), it may be seen that the scattered field in the far zone is given by

$$U_s \sim \frac{e^{ik_0 r}}{r} A(\boldsymbol{q}_1,\boldsymbol{q}_2).$$

Here $A(\boldsymbol{q}_1,\boldsymbol{q}_2)$, which is the scattering amplitude associated with the scattering of evanescent plane waves with transverse wave vector $\boldsymbol{q}_1$ into homogeneous plane waves with transverse wave vector $\boldsymbol{q}_2$, is related to the susceptibility of the scattering object by the expression

$$A(\boldsymbol{q}_1,\boldsymbol{q}_2) = k_0^2 \int d^3r \bigl(1+R(\boldsymbol{q}_2)e^{2ik_z(\boldsymbol{q}_2)z}\bigr) \exp\bigl(i\,(\boldsymbol{k}_1(\boldsymbol{q}_1)-\boldsymbol{k}_2(\boldsymbol{q}_2))\cdot\boldsymbol{r}\bigr)\eta(\boldsymbol{r}).$$

Note that this result may be rewritten in the form of the integral equation (3–4) where $A(\boldsymbol{q}_1,\boldsymbol{q}_2)$ is identified with the data function $\Phi(\boldsymbol{q}_1,\boldsymbol{q}_2)$ and

$$\kappa(\boldsymbol{q}_1,\boldsymbol{q}_2;\boldsymbol{r}) = k_0^2\bigl(1+R(\boldsymbol{q}_2)e^{2ik_z(\boldsymbol{q}_2)z}\bigr) \exp\bigl(i\,(k_z(\boldsymbol{q}_1)-k_z(\boldsymbol{q}_2))\,z\bigr).$$

3B2. Vector case. As in the scalar case, the incident field is taken to be an evanescent plane wave with polarization $E_\alpha^{(0)}$

$$E_\alpha^i(\boldsymbol{r}) = E_\alpha^{(0)} e^{i\boldsymbol{k}_1(\boldsymbol{q}_1)\cdot\boldsymbol{r}}, \tag{3–13}$$

where $\boldsymbol{k}_1(\boldsymbol{q}_1) = (\boldsymbol{q}_1, k_z(\boldsymbol{q}_1))$ is the incident wave vector and $k_0 \leq |\boldsymbol{q}_1| \leq nk_0$. In the far zone the scattered field is characterized by the wave vector $\boldsymbol{k}_2(\boldsymbol{q}_2) = (\boldsymbol{q}_2, k_z(\boldsymbol{q}_2))$ with $|\boldsymbol{q}_2| \leq k_0$. Using the integral equation (2–11) for the scattered field and (3–6), it may be seen that asymptotic form of the scattered field in the far zone is given by

$$E_\alpha^s \sim \frac{e^{ik_0 r}}{r} A_\alpha(\boldsymbol{q}_1, \boldsymbol{q}_2).$$

Here $A_\alpha(\boldsymbol{q}_1, \boldsymbol{q}_2)$ denotes the vector scattering amplitude which is related to the susceptibility by

$$A_\alpha(\boldsymbol{q}_1, \boldsymbol{q}_2) = \int d^3r\, w_{\alpha\beta}(\boldsymbol{q}_2, z) E_\beta^{(0)} \exp\bigl(i\,(\boldsymbol{k}(\boldsymbol{q}_1) - \boldsymbol{k}(\boldsymbol{q}_2))\cdot\boldsymbol{r}\bigr)\eta(\boldsymbol{r}).$$

This relation may be written in the form of the vector integral equation (3–9) where the scattering amplitude $A_\alpha(\boldsymbol{q}_1, \boldsymbol{q}_2)$ is identified with the data function $\Phi_\alpha(\boldsymbol{q}_1, \boldsymbol{q}_2)$ and

$$\kappa_\alpha(\boldsymbol{q}_1, \boldsymbol{q}_2; \boldsymbol{r}) = w_{\alpha\beta}(\boldsymbol{q}_2, z) E_\beta^{(0)} \exp\bigl(i\,(k_z(\boldsymbol{q}_1) - k_z(\boldsymbol{q}_2))\,z\bigr),$$

with $w_{\alpha\beta}$ given by (3–7).

3C. Photon Scanning Tunneling Tomography. In photon scanning tunneling tomography, the sample is illuminated by an evanescent wave and the scattered field is detected in the near zone. See Figure 1. Photon scanning tunneling tomography is a hybrid of total internal reflection tomography and scanning near-field tomography. The analyses follows those in Section 3A1 for the scalar case and in Section 3A2 for the vector case.

3C1. Scalar case. The sample is illuminated by an evanescent plane wave of the form (3–12). The scattered field is then given by (2–4). If the scattered field is sampled on the plane $z = z_d$ and the data function $\Phi(\boldsymbol{q}_1, \boldsymbol{q}_2)$ is defined by (3–5), it can be seen that

$$\Phi(\boldsymbol{q}_1, \boldsymbol{q}_2) = \left(\frac{k_0}{h}\right)^2 \int d^3r \sum_{\boldsymbol{q}} \exp\bigl(i(\boldsymbol{q}_1 - \boldsymbol{q}_2 - \boldsymbol{q})\cdot\boldsymbol{\rho}\bigr) e^{ik_z(\boldsymbol{q}_1)z} g(z_d, z; \boldsymbol{q}_2 - \boldsymbol{q})\eta(\boldsymbol{r}). \tag{3–14}$$

Note that if $\eta(\boldsymbol{r})$ is transversely band-limited then (3–14) may be put in the form of the scalar integral equation (3–4) with

$$\kappa(\boldsymbol{q}_1, \boldsymbol{q}_2; z) = \left(\frac{k_0}{h}\right)^2 e^{ik_z(\boldsymbol{q}_1)z} g(z_d, z; \boldsymbol{q}_2).$$

3C2. Vector case. The sample is illuminated with an evanescent plane wave of the form (3–13) and the scattered field is given by (2–11). The data function, defined by (3–10), may be seen to be given by

$$\Phi_\alpha(\boldsymbol{q}_1,\boldsymbol{q}_2) = \left(\frac{k_0}{h}\right)^2 \int d^3r \sum_{\boldsymbol{p}} \exp\bigl(i(\boldsymbol{q}_1-\boldsymbol{q}_2-\boldsymbol{p})\cdot\boldsymbol{\rho}\bigr) \times e^{ik_z(\boldsymbol{q}_1)z} g_{\alpha\beta}(z_d,z;\boldsymbol{q}_2-\boldsymbol{p}) E^{(0)}_\beta \eta(\boldsymbol{r}). \quad (3\text{–}15)$$

If $\eta(\boldsymbol{r})$ is transversely band-limited, then (3–15) has the form of the vector integral equation (3–9) with

$$\kappa_\alpha(\boldsymbol{q}_1,\boldsymbol{q}_2;z) = \left(\frac{k_0}{h}\right)^2 e^{ik_z(\boldsymbol{q}_1)z} g_{\alpha\beta}(z_d,z;\boldsymbol{q}_2) E^{(0)}_\beta. \quad (3\text{–}16)$$

3D. Near-Field Power Extinction Tomography. In near-field power extinction tomography, the sample is illuminated by a coherent beam consisting of a superposition of two evanescent plane waves as shown in Figure 3. The intensity of the incident field is then structured due to the interference between the plane waves as may be seen in Figure 6. Some of the power carried by the

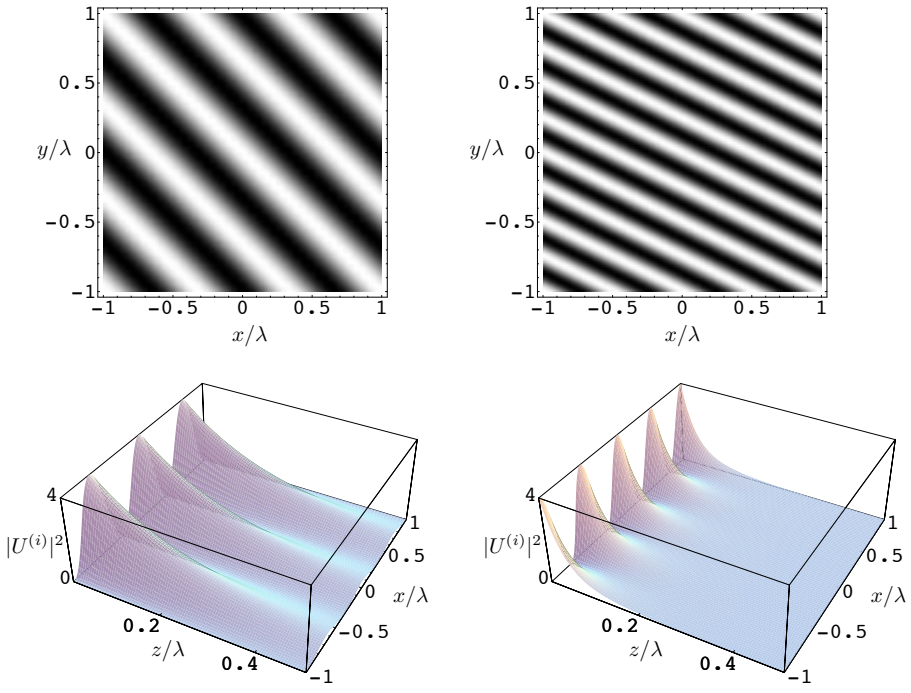

Figure 6. Two sets of two evanescent plane waves. The top row displays the intensity in the $z = 0$ plane resulting from the addition of the evanescent waves. The bottom figures display the intensity of the resultant field as a function of depth, z, and one of the transverse coordinates, x, in the $y = 0$ plane.

incident field is absorbed by the sample and some is scattered into propagating modes of the scattered field in both the upper and lower half-spaces. The total power lost from the incident field due to the presence of the sample is called the extinguished power. For the scattering of single homogeneous plane waves, the extinguished power is usually normalized by the incident power per unit area and the resulting quantity is called the total cross-section. The power extinguished from the beam is monitored at the output of the totally reflected component plane waves. To obtain the structure of the sample, the extinguished power is recorded as both the relative phase and the the orientation of the constituent evanescent waves are varied. Thus the measurements need not be phase sensitive.

3D1. Scalar case. Consider a scattering experiment with an incident field consisting of a superposition of two evanescent waves of the form

$$U_i(\boldsymbol{r}) = a_1 e^{i\boldsymbol{k}_1\cdot\boldsymbol{r}} + a_2 e^{i\boldsymbol{k}_2\cdot\boldsymbol{r}},$$

where a_1, a_2 denote the amplitudes of the waves and $\boldsymbol{k}_1, \boldsymbol{k}_2$ their wave vectors. According to the generalized optical theorem (2–5), the extinguished power is given by

$$P(a_1,a_2) = \frac{4\pi}{k_0} \times \operatorname{Im}\left(|a_1|^2 A(\boldsymbol{k}_1,\boldsymbol{k}_1^*) + a_1^* a_2 A(\boldsymbol{k}_2,\boldsymbol{k}_1^*) + a_2^* a_1 A(\boldsymbol{k}_1,\boldsymbol{k}_2^*) + |a_2|^2 A(\boldsymbol{k}_2,\boldsymbol{k}_2^*)\right). \quad (3\text{–}17)$$

Here $A(\boldsymbol{k}_1,\boldsymbol{k}_2)$ is the scattering amplitude associated with the scattering of a plane wave with wave vector $\boldsymbol{k}_1$ into a plane wave with wave vector $\boldsymbol{k}_2$. Using (2–7), it may be seen that to lowest order in $\eta(\boldsymbol{r})$

$$A(\boldsymbol{k}_1,\boldsymbol{k}_2) = k_0^2 \int d^3r e^{i(\boldsymbol{k}_1-\boldsymbol{k}_2)\cdot\boldsymbol{r}} \eta(\boldsymbol{r}). \quad (3\text{–}18)$$

It will prove useful to extract the cross-terms from (3–17), that is to gain information about the scattering amplitude for nonzero momentum transfer. This can be accomplished for any set of $\boldsymbol{k}_1$ and $\boldsymbol{k}_2$ through four measurements of the extinguished power where the relative phases are varied between measurements. To this end it is useful define the data function

$$\Phi(\boldsymbol{k}_1,\boldsymbol{k}_2) = \frac{k_0}{8\pi a_1^* a_2}\big(P(a_1,ia_2) - P(a_1,-ia_2) + i\big(P(a_1,a_2) - P(a_1,-a_2)\big)\big).$$

It may be seen from (3–17) that the data function is related to the scattering amplitude by

$$\Phi(\boldsymbol{k}_1,\boldsymbol{k}_2) = A(\boldsymbol{k}_1,\boldsymbol{k}_2^*) - A^*(\boldsymbol{k}_2,\boldsymbol{k}_1^*). \quad (3\text{–}19)$$

Let $\alpha(\boldsymbol{r}) \equiv \operatorname{Im}\eta(\boldsymbol{r})$ denote the absorptive part of the susceptibility $\eta(\boldsymbol{r})$. Then (3–18) and (3–19) yield

$$\Phi(\boldsymbol{k}_1,\boldsymbol{k}_2) = \int d^3r e^{i(\boldsymbol{k}_1-\boldsymbol{k}_2^*)\cdot\boldsymbol{r}} \alpha(\boldsymbol{r}).$$

Note that this result may be rewritten in the form of the integral equation (3–4) where

$$\kappa(\boldsymbol{q}_1, \boldsymbol{q}_2; \boldsymbol{r}) = 2ik_0^2 \exp\big(i\,(k_z(\boldsymbol{q}_1) - k_z^*(\boldsymbol{q}_2))\,z\big),$$

and the dependence of $\boldsymbol{k}_1, \boldsymbol{k}_2$ on their transverse parts $\boldsymbol{q}_1, \boldsymbol{q}_2$ has been made explicit.

3D2. Vector case. As in the scalar case the experiment consists of a sample in vacuum in the upper half-space and a set of totally internally reflected plane waves in the lower half-space where $n > 1$. The incident field on the vacuum side then consists of a coherent superposition of two evanescent waves of the form

$$\boldsymbol{E}^i = \boldsymbol{a}_1 e^{i\boldsymbol{k}_1 \cdot \boldsymbol{r}} + \boldsymbol{a}_2 e^{i\boldsymbol{k}_2 \cdot \boldsymbol{r}},$$

where $\boldsymbol{a}_1, \boldsymbol{a}_2$ denote the vector amplitudes of the waves and $\boldsymbol{k}_1, \boldsymbol{k}_2$ their wave vectors. The extinguished power is given by

$$P(\boldsymbol{a}_1, \boldsymbol{a}_2) = \frac{4\pi}{k_0} \operatorname{Im}\big(|a_1|^2 \boldsymbol{A}(\boldsymbol{k}_1, \boldsymbol{k}_1^*) \cdot \hat{\boldsymbol{e}}_1^* + a_1^* a_2 \boldsymbol{A}(\boldsymbol{k}_2, \boldsymbol{k}_1^*) \cdot \hat{\boldsymbol{e}}_1^* + a_2^* a_1 \boldsymbol{A}(\boldsymbol{k}_1, \boldsymbol{k}_2^*) \cdot \hat{\boldsymbol{e}}_2^* + |a_2|^2 \boldsymbol{A}(\boldsymbol{k}_2, \boldsymbol{k}_2^*) \cdot \hat{\boldsymbol{e}}_2^*\big), \quad (3\text{–}20)$$

where $\boldsymbol{a}_1 = a_1 \hat{\boldsymbol{e}}_1$ and $\boldsymbol{a}_2 = a_2 \hat{\boldsymbol{e}}_2$, $\hat{\boldsymbol{e}}_1, \hat{\boldsymbol{e}}_2$ denote unit vectors in the directions of $\boldsymbol{a}_1, \boldsymbol{a}_2$, and we have used the generalized optical theorem (2–12). Here, to lowest order in $\eta(\boldsymbol{r})$, the vector scattering amplitude is given by

$$\boldsymbol{A}(\boldsymbol{k}_1, \boldsymbol{k}_2) = \frac{k_0^2 c}{8\pi}\, \hat{\boldsymbol{e}} \int d^3 r e^{i(\boldsymbol{k}_1 - \boldsymbol{k}_2)\cdot \boldsymbol{r}} \eta(\boldsymbol{r}).$$

Note that within the first Born approximation $\boldsymbol{A}(\boldsymbol{k}_1, \boldsymbol{k}_2) \cdot \hat{\boldsymbol{e}} = c/8\pi A(\boldsymbol{k}_1, \boldsymbol{k}_2)$, where $A(\boldsymbol{k}_1, \boldsymbol{k}_2)$ is the scalar scattering amplitude defined in (3–18).

The data function $\Phi(\boldsymbol{k}_1, \boldsymbol{k}_2)$ is defined by

$$\Phi(\boldsymbol{k}_1, \boldsymbol{k}_2) = \frac{k_0}{c\, \boldsymbol{a}_1^* \cdot \boldsymbol{a}_2} \times \big(P(\boldsymbol{a}_1, i\boldsymbol{a}_2) - P(\boldsymbol{a}_1, -i\boldsymbol{a}_2) + i\big(P(\boldsymbol{a}_1, \boldsymbol{a}_2) - P(\boldsymbol{a}_1, -\boldsymbol{a}_2)\big)\big). \quad (3\text{–}21)$$

Then it is readily seen, within the accuracy of the first Born approximation, that $\Phi(\boldsymbol{k}_1, \boldsymbol{k}_2)$ is related to the scalar scattering amplitude by

$$\Phi(\boldsymbol{k}_1, \boldsymbol{k}_2) = A(\boldsymbol{k}_1, \boldsymbol{k}_2^*) - A^*(\boldsymbol{k}_2, \boldsymbol{k}_1^*).$$

This result is identical to (3–19). As a consequence, with suitable modifications we may apply the scalar theory to vector near-field power extinction tomography.

4. Inverse Problem

The inverse problem consists of recovering the susceptibility $\eta(\boldsymbol{r})$ from the data function $\Phi(\boldsymbol{q}_1, \boldsymbol{q}_2)$. To this end, the pseudoinverse solution to the integral equations (3–4) and (3–9) will be systematically constructed. First, a brief review the singular value decomposition (SVD) of linear operators on Hilbert spaces[49] is given.

4A. Singular Value Decomposition. Let K denote a linear operator with kernel $K(x, y)$ which maps the Hilbert space $\mathcal{H}_1$ into the Hilbert space $\mathcal{H}_2$. The SVD of K is a representation of the form

$$K(x, y) = \sum_n \sigma_n g_n(x) f_n^*(y),$$

where σ_n is the singular value associated with the singular functions f_n and g_n. The $\{f_n\}$ and $\{g_n\}$ are orthonormal bases of $\mathcal{H}_1$ and $\mathcal{H}_2$, respectively and are eigenfunctions with eigenvalues σ_n^2 of the positive self-adjoint operators K^*K and KK^*:

$$K^*K f_n = \sigma_n^2 f_n, \qquad KK^* g_n = \sigma_n^2 g_n.$$

In addition, the f_n and g_n are related by

$$K f_n = \sigma_n g_n, \qquad K^* g_n = \sigma_n f_n.$$

The pseudoinverse solution to the equation $Kf = g$ is defined to be the minimizer of $\|Kf - g\|$ with smallest norm. This well-defined element $f^+ \in N(K)^\perp$ is unique and may be shown[49] to be of the form $f^+ = K^+ g$, where the pseudoinverse operator K^+ is given by $K^+ = K^*(KK^*)^{-1}$ and $N(K)^\perp$ is the orthogonal complement of the null space of K. The SVD of K may be used to express K^+ as

$$K^+(x, y) = \sum_n \frac{1}{\sigma_n} f_n(x) g_n^*(y). \tag{4–1}$$

4B. Scalar Case. Consider the scalar integral equation

$$\Phi(\boldsymbol{q}_1, \boldsymbol{q}_2) = \int d^3 r K(\boldsymbol{q}_1, \boldsymbol{q}_2; \boldsymbol{r}) \eta(\boldsymbol{r}),$$

where

$$K(\boldsymbol{q}_1, \boldsymbol{q}_2; \boldsymbol{r}) = \exp\big(i(\boldsymbol{q}_1 - \boldsymbol{q}_2) \cdot \boldsymbol{\rho}\big) \kappa(\boldsymbol{q}_1, \boldsymbol{q}_2; z).$$

This equation describes the scalar forward problem for each of the experimental modalities we have considered. In each case, only the functional form of $\kappa(\boldsymbol{q}_1, \boldsymbol{q}_2; z)$ must be altered. In addition, the wave vectors $\boldsymbol{q}_1, \boldsymbol{q}_2$ take values in a set which depends upon the choice of experiment and the available data. It is convenient to introduce a data set $\mathcal{Q}$ that specifies the available wave vectors and a function $\chi(\boldsymbol{q}_1, \boldsymbol{q}_2)$ that is unity if $(\boldsymbol{q}_1, \boldsymbol{q}_2) \in \mathcal{Q}$ and is zero otherwise. The function $\kappa(\boldsymbol{q}_1, \boldsymbol{q}_2; z)$ is then modified so that $\kappa(\boldsymbol{q}_1, \boldsymbol{q}_2; z) \to \kappa(\boldsymbol{q}_1, \boldsymbol{q}_2; z)\chi(\boldsymbol{q}_1, \boldsymbol{q}_2)$.

To obtain the SVD of $K(\boldsymbol{q}_1, \boldsymbol{q}_2; \boldsymbol{r})$ it will prove useful to introduce the following identity:

$$K(\boldsymbol{q}_1, \boldsymbol{q}_2; \boldsymbol{r}) = \int d^2Q \exp(i\boldsymbol{Q} \cdot \boldsymbol{\rho}) \delta(\boldsymbol{Q} + \boldsymbol{q}_2 - \boldsymbol{q}_1) \kappa(\boldsymbol{Q} + \boldsymbol{q}_2, \boldsymbol{q}_2; z).$$

Using this result, the matrix elements of the operator KK^* are seen to be given by

$$KK^*(\boldsymbol{q}_1, \boldsymbol{q}_2; \boldsymbol{q}_1', \boldsymbol{q}_2') = \int d^2Q M(\boldsymbol{q}_2, \boldsymbol{q}_2'; \boldsymbol{Q}) \delta(\boldsymbol{Q} + \boldsymbol{q}_2 - \boldsymbol{q}_1) \delta(\boldsymbol{Q} + \boldsymbol{q}_2' - \boldsymbol{q}_1'), \quad (4\text{–}2)$$

where

$$M(\boldsymbol{q}_2, \boldsymbol{q}_2'; \boldsymbol{Q}) = \int_0^L dz \kappa(\boldsymbol{Q} + \boldsymbol{q}_2, \boldsymbol{q}_2; z) \kappa^*(\boldsymbol{Q} + \boldsymbol{q}_2', \boldsymbol{q}_2'; z),$$

with L the range of $\eta(\boldsymbol{r})$ in the $\hat{\boldsymbol{z}}$ direction. The singular vectors $g_{\boldsymbol{Q}\boldsymbol{Q}'}$ of K satisfy

$$KK^* g_{\boldsymbol{Q}\boldsymbol{Q}'} = \sigma^2_{\boldsymbol{Q}\boldsymbol{Q}'} g_{\boldsymbol{Q}\boldsymbol{Q}'},$$

and may be constructed by making the *ansatz* that

$$g_{\boldsymbol{Q}\boldsymbol{Q}'}(\boldsymbol{q}_1, \boldsymbol{q}_2) = C_{\boldsymbol{Q}'}(\boldsymbol{q}_2; \boldsymbol{Q}) \delta(\boldsymbol{Q} + \boldsymbol{q}_2 - \boldsymbol{q}_1), \quad (4\text{–}3)$$

for some $C_{\boldsymbol{Q}'}(\boldsymbol{q}_2; \boldsymbol{Q})$. Equation (4–2) now implies that

$$\int d^2q' M(\boldsymbol{q}, \boldsymbol{q}'; \boldsymbol{Q}) C_{\boldsymbol{Q}'}(\boldsymbol{q}'; \boldsymbol{Q}) = \sigma^2_{\boldsymbol{Q}\boldsymbol{Q}'} C_{\boldsymbol{Q}'}(\boldsymbol{q}; \boldsymbol{Q}).$$

Thus $C_{\boldsymbol{Q}'}(\boldsymbol{q}_2; \boldsymbol{Q})$ is an eigenvector of $M(\boldsymbol{Q})$ labeled by $\boldsymbol{Q}'$ with eigenvalue $\sigma^2_{\boldsymbol{Q}\boldsymbol{Q}'}$. Since $M(\boldsymbol{Q})$ is self-adjoint, the $C_{\boldsymbol{Q}'}(\boldsymbol{q}_2; \boldsymbol{Q})$ may be taken to orthonormal. Next, the $f_{\boldsymbol{Q}\boldsymbol{Q}'}$ may be found from $K^* g_{\boldsymbol{Q}\boldsymbol{Q}'} = \sigma_{\boldsymbol{Q}\boldsymbol{Q}'} f_{\boldsymbol{Q}\boldsymbol{Q}'}$ and are given by

$$f_{\boldsymbol{Q}\boldsymbol{Q}'}(\boldsymbol{r}) = \frac{1}{\sigma_{\boldsymbol{Q}\boldsymbol{Q}'}} \int d^2q \exp(-i\boldsymbol{Q} \cdot \boldsymbol{\rho}) \kappa^*(\boldsymbol{Q} + \boldsymbol{q}, \boldsymbol{q}; z) C^*_{\boldsymbol{Q}'}(\boldsymbol{q}; \boldsymbol{Q}). \quad (4\text{–}4)$$

It follows that the SVD of $K(\boldsymbol{q}_1, \boldsymbol{q}_2; \boldsymbol{r})$ is given by the expression

$$K(\boldsymbol{q}_1, \boldsymbol{q}_2; \boldsymbol{r}) = \int d^2Q d^2Q' \sigma_{\boldsymbol{Q}\boldsymbol{Q}'} f^*_{\boldsymbol{Q}\boldsymbol{Q}'}(\boldsymbol{r}) g_{\boldsymbol{Q}\boldsymbol{Q}'}(\boldsymbol{q}_1, \boldsymbol{q}_2). \quad (4\text{–}5)$$

The SVD (4–5) may now be used to obtain the pseudoinverse solution to the integral equation (3–4):

$$\eta^+(\boldsymbol{r}) = \int d^2q_1 d^2q_2 K^+(\boldsymbol{r}; \boldsymbol{q}_1, \boldsymbol{q}_2) \Phi(\boldsymbol{q}_1, \boldsymbol{q}_2),$$

where $K^+(\boldsymbol{r}; \boldsymbol{q}_1, \boldsymbol{q}_2)$ is the pseudoinverse of $K(\boldsymbol{q}_1, \boldsymbol{q}_2; \boldsymbol{r})$. Using the result (4–1), the pseudoinverse K^+ may be seen to be given by

$$K^+(\boldsymbol{r}; \boldsymbol{q}_1, \boldsymbol{q}_2) = \int d^2Q d^2Q' \frac{1}{\sigma_{\boldsymbol{Q}\boldsymbol{Q}'}} f_{\boldsymbol{Q}\boldsymbol{Q}'}(\boldsymbol{r}) g^*_{\boldsymbol{Q}\boldsymbol{Q}'}(\boldsymbol{q}_1, \boldsymbol{q}_2). \quad (4\text{–}6)$$

Substituting (4–3) and (4–4) into (4–6) and using the spectral decomposition

$$\int d^2Q' \frac{1}{\sigma^2_{\boldsymbol{Q}\boldsymbol{Q}'}} C_{\boldsymbol{Q}'}(\boldsymbol{q};\boldsymbol{Q}) C^*_{\boldsymbol{Q}'}(\boldsymbol{q}';\boldsymbol{Q}) = M^{-1}(\boldsymbol{q},\boldsymbol{q}';\boldsymbol{Q}),$$

where $M^{-1}(\boldsymbol{q},\boldsymbol{q}';\boldsymbol{Q})$ is the $\boldsymbol{q}\boldsymbol{q}'$ matrix element of $M^{-1}(\boldsymbol{Q})$ we obtain

$$\eta^+(\boldsymbol{r}) = \int d^2q_1 d^2q_2 d^2q_2' \int d^2Q \exp(-i\boldsymbol{Q}\cdot\boldsymbol{\rho})\,\delta(\boldsymbol{Q}+\boldsymbol{q}_2-\boldsymbol{q}_1) \times M^{-1}(\boldsymbol{q}_2,\boldsymbol{q}_2';\boldsymbol{Q})\kappa^*(\boldsymbol{Q}+\boldsymbol{q}_2',\boldsymbol{q}_2';z)\Phi(\boldsymbol{q}_1,\boldsymbol{q}_2), \quad (4\text{–}7)$$

which is the inversion formula for scalar near-field tomography.

4C. Vector Case. Consider the vector integral equation

$$\Phi_\alpha(\boldsymbol{q}_1,\boldsymbol{q}_2) = \int d^3r K_\alpha(\boldsymbol{q}_1,\boldsymbol{q}_2;\boldsymbol{r})\eta(\boldsymbol{r}),$$

where

$$K_\alpha(\boldsymbol{q}_1,\boldsymbol{q}_2;\boldsymbol{r}) = \exp\big(i(\boldsymbol{q}_1-\boldsymbol{q}_2)\cdot\boldsymbol{\rho}\big)\kappa_\alpha(\boldsymbol{q}_1,\boldsymbol{q}_2;z).$$

The functional form of $\kappa_\alpha(\boldsymbol{q}_1,\boldsymbol{q}_2;\boldsymbol{r})$ is determined by the experimental modality which is under consideration. As in the scalar case, it is assumed that $\Phi_\alpha(\boldsymbol{q}_1,\boldsymbol{q}_2)$ is specified for $(\boldsymbol{q}_1,\boldsymbol{q}_2)$ in some data set and an appropriate blocking function $\chi(\boldsymbol{q}_1,\boldsymbol{q}_2)$ is introduced. The vector integral equation (3–9) differs from its scalar counterpart (3–4) only by a factor associated with the polarization. Evidently, by measuring a fixed component of the scattered field we see that the scalar inversion formula (4–7) may be used to reconstruct $\eta(\boldsymbol{r})$.

The SVD for the general vector case may be obtained by an analysis similar to the scalar case. Following the previous development it may be seen that the SVD of $K_\alpha(\boldsymbol{q}_1,\boldsymbol{q}_2;\boldsymbol{r})$ takes the form

$$K_\alpha(\boldsymbol{q}_1,\boldsymbol{q}_2;\boldsymbol{r}) = \int d^2Q d^2Q' \sigma_{\boldsymbol{Q}\boldsymbol{Q}'} f^*_{\boldsymbol{Q}\boldsymbol{Q}'}(\boldsymbol{r}) g^\alpha_{\boldsymbol{Q}\boldsymbol{Q}'}(\boldsymbol{q}_1,\boldsymbol{q}_2).$$

Here the singular functions are given by

$$g^\alpha_{\boldsymbol{Q}\boldsymbol{Q}'}(\boldsymbol{q}_1,\boldsymbol{q}_2) = C^\alpha_{\boldsymbol{Q}'}(\boldsymbol{q}_2;\boldsymbol{Q})\delta(\boldsymbol{Q}+\boldsymbol{q}_2-\boldsymbol{q}_1),$$
$$f_{\boldsymbol{Q}\boldsymbol{Q}'}(\boldsymbol{r}) = \frac{1}{\sigma_{\boldsymbol{Q}\boldsymbol{Q}'}} \int d^2q \exp(-i\boldsymbol{Q}\cdot\boldsymbol{\rho})\kappa^*_\alpha(\boldsymbol{Q}+\boldsymbol{q},\boldsymbol{q};z) C^{\alpha *}_{\boldsymbol{Q}'}(\boldsymbol{q};\boldsymbol{Q}).$$

The $C^\alpha_{\boldsymbol{Q}'}(\boldsymbol{q}_2;\boldsymbol{Q})$ are eigenfuntions of $M_{\alpha\beta}(\boldsymbol{q}_2,\boldsymbol{q}_2';\boldsymbol{Q})$ with eigenvalues $\sigma^2_{\boldsymbol{Q}\boldsymbol{Q}'}$

$$\int d^2q' M_{\alpha\beta}(\boldsymbol{q},\boldsymbol{q}';\boldsymbol{Q}) C^\beta_{\boldsymbol{Q}'}(\boldsymbol{q}';\boldsymbol{Q}) = \sigma^2_{\boldsymbol{Q}\boldsymbol{Q}'} C^\alpha_{\boldsymbol{Q}'}(\boldsymbol{q};\boldsymbol{Q}),$$

where

$$M_{\alpha\beta}(\boldsymbol{q}_2,\boldsymbol{q}_2';\boldsymbol{Q}) = \int_0^L dz \kappa_\alpha(\boldsymbol{Q}+\boldsymbol{q}_2,\boldsymbol{q}_2;z)\kappa^*_\beta(\boldsymbol{Q}+\boldsymbol{q}_2',\boldsymbol{q}_2';z).$$

The pseudoinverse solution to the integral equation (3–9) is given by

$$\eta^+(\boldsymbol{r}) = \int d^2q_1 d^2q_2 K_\alpha^+(\boldsymbol{r};\boldsymbol{q}_1,\boldsymbol{q}_2)\Phi_\alpha(\boldsymbol{q}_1,\boldsymbol{q}_2),$$

where

$$K_\alpha^+(\boldsymbol{r};\boldsymbol{q}_1,\boldsymbol{q}_2) = \int d^2Q d^2Q' \frac{1}{\sigma_{\boldsymbol{QQ}'}} f_{\boldsymbol{QQ}'}(\boldsymbol{r}) g^{\alpha *}_{\boldsymbol{QQ}'}(\boldsymbol{q}_1,\boldsymbol{q}_2).$$

More explicitly,

$$\eta^+(\boldsymbol{r}) = \int d^2q_1 d^2q_2 d^2q_2' \int d^2Q \exp(-i\boldsymbol{Q}\cdot\boldsymbol{\rho})\,\delta(\boldsymbol{Q}+\boldsymbol{q}_2-\boldsymbol{q}_1) \times \left(M^{-1}(\boldsymbol{Q})\right)_{\alpha\beta}(\boldsymbol{q}_2,\boldsymbol{q}_2')\kappa_\alpha^*(\boldsymbol{Q}+\boldsymbol{q}_2',\boldsymbol{q}_2';z)\Phi_\beta(\boldsymbol{q}_1,\boldsymbol{q}_2), \quad (4\text{–}8)$$

which is the inversion formula for vector near-field tomography.

4D. Regularization and Resolution. In order to avoid numerical instabilty and set the resolution of the reconstructed image to be comensurate with the available data, the SVD inversion formulas must be regularized. In particular, $1/\sigma$ is replaced in the inversion formulas (4–7) and (4–8) by $R(\sigma)$ where $R(\sigma)$ is a suitable regularizer The role of regularization is to limit the contribution of small singular values to the reconstruction. This has the effect of replacing an ill-posed problem with a well-posed one that closely approximates the original. A simple choice for $R(\sigma)$ consists of truncation, that is,

$$R(\sigma_{\boldsymbol{QQ}'}) = \begin{cases} \sigma^{-1}_{\boldsymbol{QQ}'} & \text{if } \sigma_{\boldsymbol{QQ}'} \geq \sigma_{\min}, \\ 0 & \text{if } \sigma_{\boldsymbol{QQ}'} < \sigma_{\min}. \end{cases}$$

for some σ_{min}. If Tikhonov regularization is used

$$R(\sigma_{\boldsymbol{QQ}'}) = \frac{\sigma_{\boldsymbol{QQ}'}}{\lambda + \sigma^2_{\boldsymbol{QQ}'}},$$

where λ is the regularization parameter. This choice leads to smoothing of $\eta^+(\boldsymbol{r})$ by penalizing functions with large L^2 norm. Other regularization schemes may be appropriate depending on the noise model and experimental particulars.

Regularization effectively filters the reconstructed image. In the near-field inverse scattering problem, the evanescent waves that decay most rapidly tend to be filtered out. Since the most rapidly decaying evanescent waves are also the waves on which the high spatial frequency information is encoded, regularization limits the resolution achievable.

4E. Numerical Simulations. The preceding results may be better understood with the aid of numerical simulations of reconstructions in several different forms of near-field tomography. Collection mode scalar near-field scanning tomography is considered first [26]. The model system consists of a three-dimensional distribution of six point scatterers, two on the horizontal, vertical or diagonal axis of each of three planes as shown in Figure 2. For simplicity the indices of refraction of both half-spaces are chosen to have the vacuum value of unity. The field was

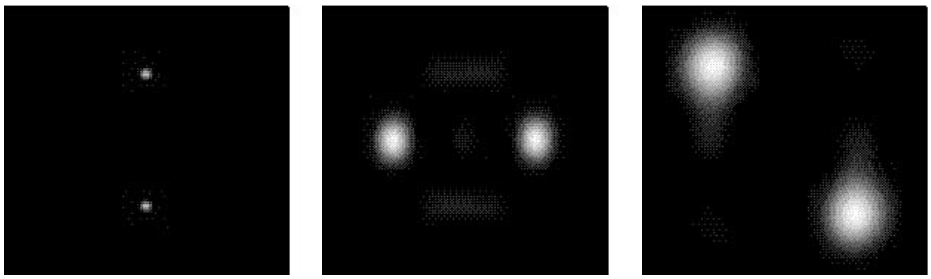

Figure 7. Reconstructed tomographs of the scattering object shown in Figure 2.

sampled on a lattice with spacing $\lambda/20$ and the sample was illuminated with 21 different plane waves. Figure 7 shows the reconstructions obtained. Observe that the simulated NSOM image obtained with the tip withdrawn a distance $\lambda/4$ from the nearest plane of scatterers, as shown in Figure 2, is blurred, whereas the scatterers in the reconstructions are clearly identifiable. Because the high frequency components of the field fall off exponentially with distance from the scatterer, the resolution of the image is dependent on the depth of the slice, the deeper layers being less well resolved.

Figure 8 explores the robustness of the inversion procedure in the presence of noise [26]. Two point scatterers are located a distance 0.51λ from the scan plane with noise added to the signal at various levels as indicated. The noise was taken to be Gaussian and of zero mean, with a variance proportional to the square of the signal at each pixel on the measurement plane.

Next, total internal reflection tomography with scalar waves is considered. The reconstruction of $\eta(\boldsymbol{r})$ for a collection of spherical scatterers was performed. The forward data was calculated by considering the scattering of evanescent waves from a homogeneous sphere including multiple scattering by means of a partial wave expansion. For a sphere of radius a centered at $\boldsymbol{r}_0$ with refractive index n, it may be found that

$$A(\boldsymbol{k}_1, \boldsymbol{k}_2) = \exp(i(\boldsymbol{k}_1 - \boldsymbol{k}_2) \cdot \boldsymbol{r}_0) \sum_{\ell=0}^{\infty} (2\ell + 1) A_\ell P_\ell(\hat{\boldsymbol{k}}_1 \cdot \hat{\boldsymbol{k}}_2), \qquad (4\text{–}9)$$

where A_ℓ are the usual partial wave expansion coefficients(see, for instance [50]), P_ℓ are the Legendre polynomials and the caret has the meaning $\hat{\boldsymbol{k}} = \boldsymbol{k}/\sqrt{\boldsymbol{k} \cdot \boldsymbol{k}^*}$. To treat the scattering of evanescent waves, the argument of the Legendre polynomials in (4–9) must exceed unity. The series may nonetheless be shown to be convergent due to the rapid decay of the A_ℓ with increasing ℓ.

The forward data was obtained for a collection of four spheres of radius $\lambda/20$. All scatterers are present simultaneously in the forward simulation with inter-sphere scattering neglected. The spheres were arranged in two layers, one equatorial plane coincident with the $z = \lambda/20$ plane, the other with the $z = \lambda/4$ plane. In each layer, one sphere was taken to have index $n = 1.2$ and one sphere

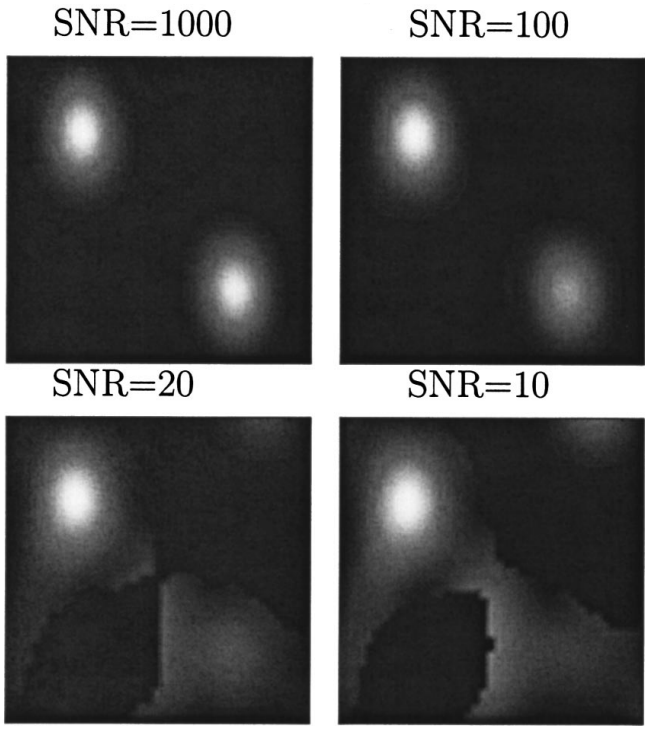

Figure 8. Demonstrating reconstruction from noisy data sets. The SNR is the ratio of the magnitude of the signal to the standard deviation of the noise at each data point. The noise in the data set for each image in identical except for a scale factor.

was taken to have index $n = 1.2 + 0.2i$. In each of the simulations complex Gaussian noise of zero mean was added to the signal at various levels as indicated. Simulations were performed for two different prisms, one (Figure 9) with an index of $n = 10$, as might be encountered in the infrared, and another (Figure 10) with an index of $n = 4$. Further details are available in [25].

It may be seen from the reconstructions that the real and imaginary parts of the susceptibility may be found separately and that the reconstructions are subwavelength resolved. The resolution depends both on the size of the regulariztion parameter that indirectly sets the number of singular functions used in the reconstruction, and on the depth, a consequence of the fact that the probe fields decay exponentially into the sample resulting in the loss of high frequency Fourier components of the susceptibility. The tomographs at the $z = \lambda/20$ layer are more highly resolved for the higher index prism than the lower index prism, but there is little difference at the $z = \lambda/4$ layer.

Next considered is photon scanning tunneling tomography for vector waves. Two point scatterers are located on the prism face separated by 0.3λ. The field and intensity were computed in the measurement plane for three scan heights,

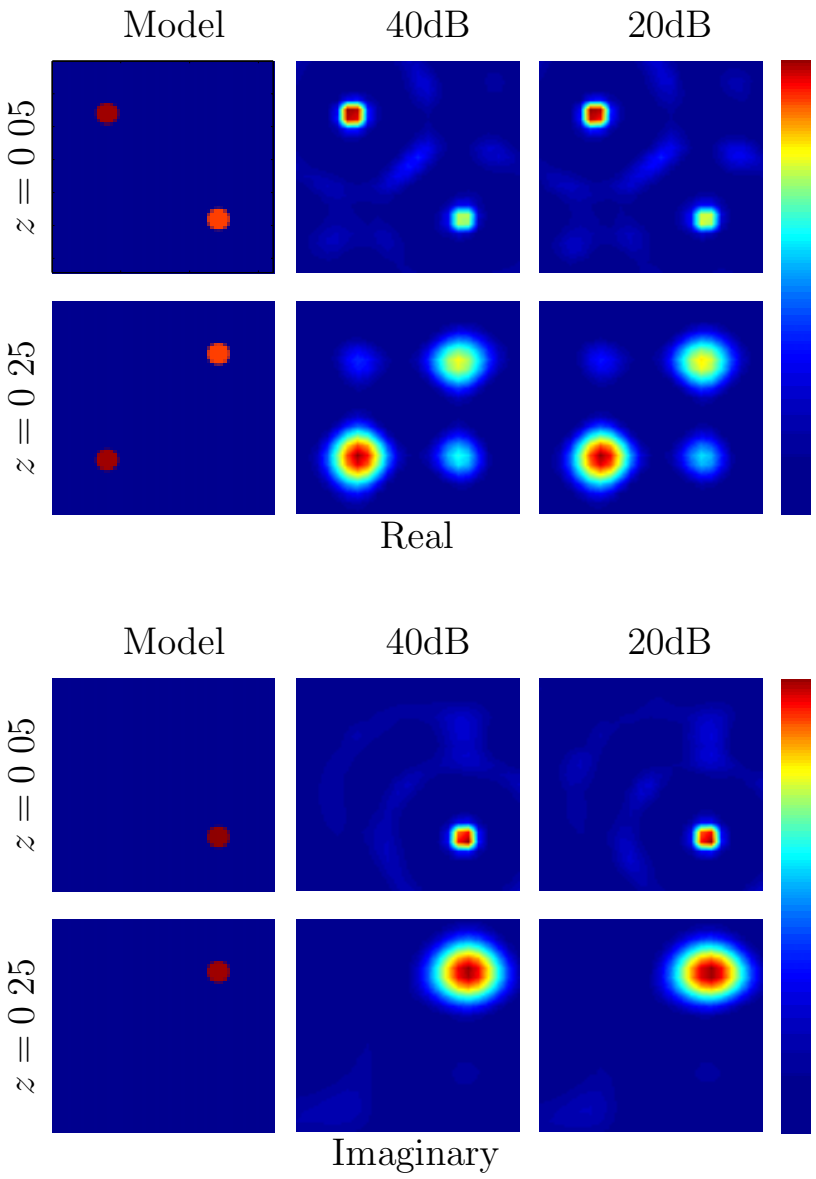

Figure 9. The reconstructed tomographs of the real and imaginary parts of the susceptibility using a prism of refractive index $n = 10$. The signal to noise ratio is given in dB above each column. The images were plotted using the linear color scale indicated to the right. The field of view in each image is $\lambda \times \lambda$.

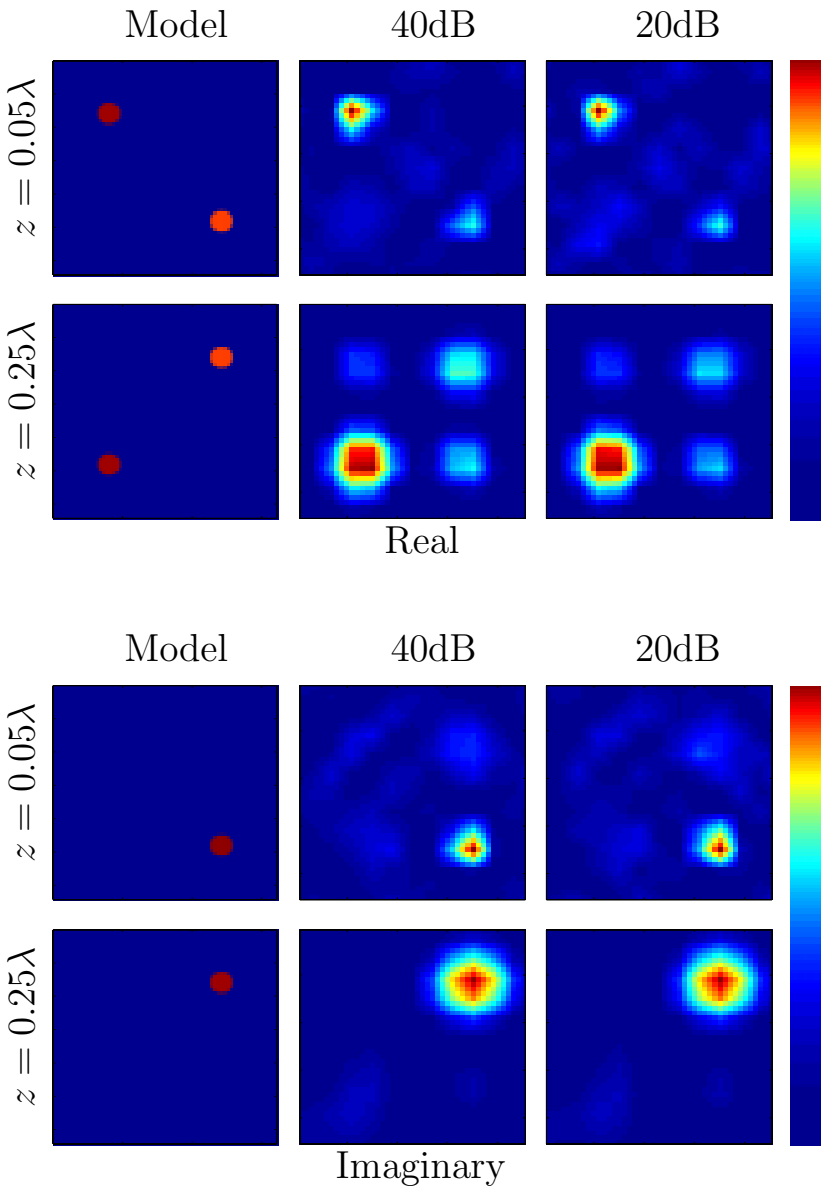

Figure 10. The reconstructed tomographs of the real and imaginary parts of the susceptibility using a prism of refractive index $n = 4$. All other parameters are as indicated in Figure 9.

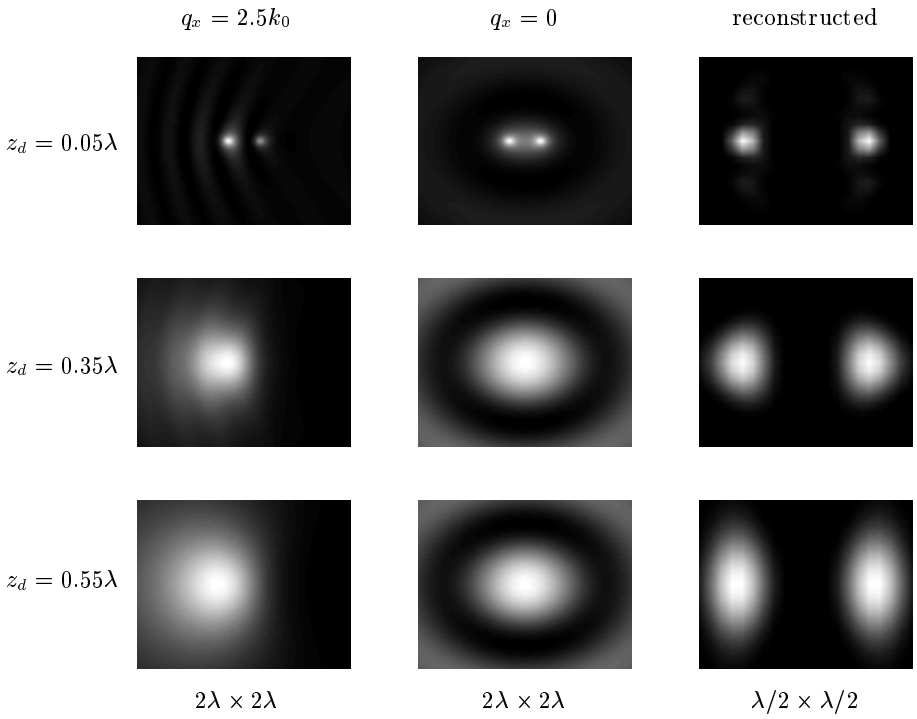

Figure 11. Demonstrating the observable intensities and reconstructed images for two point scatterers separated by 0.3λ with the measurement plane at various distances from the prism face. The left column shows the simulated intensity in the measurement plane $z = z_d$ for an illuminating field with transverse wave vector, q_x set to the maximum value attainable in a prism with index $n = 2.5$. The middle column shows the simulated intensity with the illuminating wave incident normal to the plane of observation. The right column displays the image reconstructed from multiple views obtained with different illuminating fields. Note that the images of the intensity are shown with a $2\lambda \times 2\lambda$ field of view while the reconstructed image is shown with a $\lambda/2 \times \lambda/2$ field of view.

z_d, of the probe. Only the TE polarization, *i.e.* the polarization vector parallel to the prism face, is used. The scattered field is computed on a $4\lambda \times 4\lambda$ window and sampled on a cartesian grid at a spacing of $\lambda/10$ with a total of 41 illuminating plane waves all with $q_y = 0$ and q_x on equally spaced points in the range $[-2.5k_0, 2.5k_0]$, corresponding to a range attainable with a prism of index $n = 2.5$. The computed fields are shown in Figure 11 in a $2\lambda \times 2\lambda$ field of view, while the reconstructed scatterer is shown in a $\lambda/2 \times \lambda/2$ field of view. The scan made furthest from the prism face with an illuminating evanescent wave may be seen to be dominated by the scattered wave due to the exponential decay of the illuminating field. It may be observed that the object structure, which is unclear in the direct measurements made farthest from the sample, is still clearly evident in the reconstructions. The increased spread of the points may

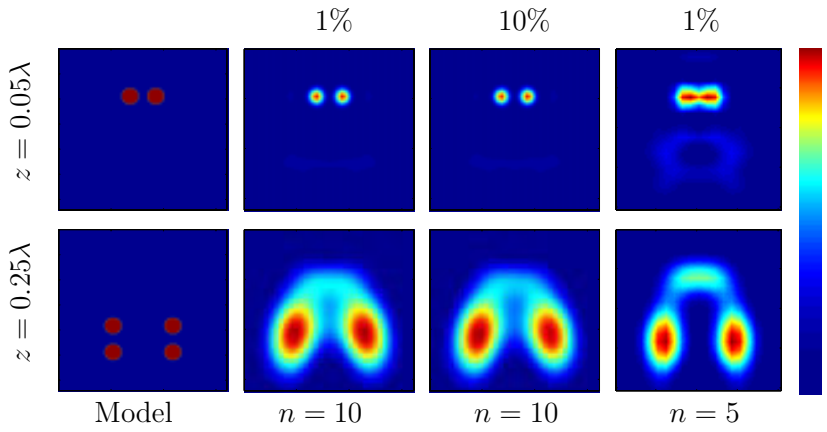

Figure 12. The simulated tomographs in power extinction tomography. The field of view is $\lambda \times \lambda$ in each image. The scatterers used in the forward simulation are shown in the column labeled Model. The numbers across the top indicate the level of noise relative to the signal. The indices listed across the bottom indicate the index of refraction of the prism used in the simulations. Each reconstruction was normalized by its maximum value and imaged using the linear color scale shown to the right.

be attributed to the loss of high spatial frequency components of the scattered field to exponential decay of evanescent waves. See [27] for further information.

Finally, reconstructions for near-field power extinction tomography with scalar waves are simulated. To demonstrate the feasibility of the inversion, the reconstruction of $\alpha(\boldsymbol{r})$ for a collection of spherical scatterers have been numerically simulated. The forward data was calculated from the partial wave expansion (4–9). The forward data was obtained for a collection of six spheres of radius $\lambda/20$ and index of refraction $n = 1.1 + 0.2i$, distributed on three planes as shown in Figure 12. All scatterers are present simultaneously in the forward simulation with inter-sphere scattering neglected. Simulations of experiments done with two different prisms, one with index of refraction $n = 5$ the other with $n = 10$ are presented. The reconstructions obtained at depths of $.05\lambda$, and $.25\lambda$ which correspond to the two separate equatorial planes of the original distribution of scatterers are displayed. Complex Gaussian noise of zero mean was added to the data function at various levels as indicated.

The resolution of the reconstruction is seen to be controlled by several factors including the index of the prism, the depth of the slice, and choice of regularization parameters. These effects may be understood by observing that the resolution is governed by the low pass filtering that is inherent in the transverse Fourier integral in (4–7) and additionally by the exponential decay of high-frequency components of the scattered field with increasing degree of evanescence. In general, a useful rule of thumb is that for a prism of index n the transverse resolution will be on the order of $\lambda/2n$ at a depth of $\lambda/2n$ after which it falls off linearly.

This is seen in the $n = 10$ simulations where the spheres whose edges are separated by $\lambda/20$ may be resolved in the slice at a depth of $\lambda/20$. However, the spheres in the next layer at $\lambda/4$ with the same spacing are not resolvable, but the groups of spheres which are spaced at $\lambda/4$ may be resolved. For the $n = 5$ case the scatterers in the top layer are not as well resolved, but the scatterers in the deeper layer are well resolved. It may be observed that the reconstruction algorithm is very robust in the presence of noise. See [51] for additional details.

5. Discussion

The mathematical structure of the near-field inverse scattering problem has been reviewed. It has been demonstrated that in the weak scattering limit, where the forward scattering problem may be linearized, an analytic solution to the inverse problem may be obtained. The data required to implement this method may be obtained from a variety of near-field optical experiments.

Several directions for further research are apparent. The solution to the inverse problem discussed here is based on a linearization of the forward probem by means of the first Born approximation. A solution applicable when multiple scattering becomes significant is desirable. An interesting novel method for inverse scattering in diffusion tomography beyond the linear model has recently been developed [52]. Diffusion tomography shares a great deal of formal mathematical structure with the near-field problem and so it may be possible to apply that method to near-field tomography. The treatment of sampling given here is adequate and outlines the basic approach, but more sophisticated sampling schemes, possibly even adaptive sampling methods, will need to be explored. Prior constraints on the sample may be used to great advantage in the inverse problem. In the work presented here, the finite thickness of the sample is always incorporated in the solution to the inverse problem. Such prior knowledge lends stability to the solution to the inverse problem and greatly improves the imaging of those parts of the sample farthest from the scan plane or the prism face. Methods to include other prior information may be expected to be similarly useful.

Near-field tomography offers improved imaging tools for a wide range of disciplines including the rapidly developing areas of research in nanotechnology. Applications may also be found in nonimaging optics as well. For instance, near-field tomography may provide a means to read out three dimensional optical data storage devices with data encoded on sub-wavelength scales. Beyond these applications, the work presented here provides new insight into the physics of highly localized wave fields and the propagation of light on very small scales.

Acknowledgments

Much of the work described in this review was carried out while we were members of the Department of Electrical Engineering at Washington University in St. Louis. We would like to express our gratitude to Professors J. A. O'Sullivan, D. L. Snyder, and B. E. Spielman for their support. It is also a pleasure to thank Professor V. A. Markel for stimulating discussions. PSC wishes to acknowledge support from the US National Aeronautics and Space Administration under Grant NAG3-2764.

Appendix

The scalar Green's function in the half-space geometry is given by

$$G(\boldsymbol{r},\boldsymbol{r}') = \frac{i}{2\pi}\int d^2q\, k_z^{-1}(\boldsymbol{q})\big\{1 + R(\boldsymbol{q})\exp\big(2ik_z(\boldsymbol{q})z'\big)\big\}\exp\big(i\boldsymbol{k}(\boldsymbol{q})\cdot(\boldsymbol{r}-\boldsymbol{r}')\big).$$

Here $R(\boldsymbol{q})$ is the reflection coefficient

$$R(\boldsymbol{q}) = \frac{k_z(\boldsymbol{q}) - k_z'(\boldsymbol{q})}{k_z(\boldsymbol{q}) + k_z'(\boldsymbol{q})},$$

with $k_z(\boldsymbol{q}) = \sqrt{k_0^2 - q^2}$, $k_z'(\boldsymbol{q}) = \sqrt{n^2k_0^2 - q^2}$, and $\boldsymbol{k}(\boldsymbol{q}) = (\boldsymbol{q}, k_z(\boldsymbol{q}))$.

The Green's tensor in the half-space geometry is given by

$$G_{\alpha\beta}(\boldsymbol{r},\boldsymbol{r}') = \frac{i}{2\pi}\int \frac{d^2q}{k_z(\boldsymbol{q})} S^{-1}_{\alpha\gamma}(\boldsymbol{q})\tilde{g}_{\gamma\delta}(\boldsymbol{q})S_{\delta\beta}(\boldsymbol{q})\exp\big(i\boldsymbol{k}(\boldsymbol{q})\cdot(\boldsymbol{r}-\boldsymbol{r}')\big),$$

where $S(\boldsymbol{q})$ is the matrix that rotates $\boldsymbol{k}(\boldsymbol{q})$ into the xz plane, or more explicitly

$$S(\boldsymbol{q}) = |\boldsymbol{q}|^{-1}\begin{pmatrix} q_x & q_y & 0 \\ -q_y & q_x & 0 \\ 0 & 0 & |\boldsymbol{q}| \end{pmatrix}$$

and

$$\begin{aligned}
\tilde{g}_{xx} &= \left(\frac{k_z(\boldsymbol{q})}{k_0}\right)^2\big(1 + R'(\boldsymbol{q})\exp(2ik_z(\boldsymbol{q})z')\big),\\
\tilde{g}_{yy} &= 1 + R(\boldsymbol{q})\exp(2ik_z(\boldsymbol{q})z'),\\
\tilde{g}_{zz} &= \left(\frac{|\boldsymbol{q}|}{k_0}\right)^2\big(1 - R'(\boldsymbol{q})\exp(2ik_z(\boldsymbol{q})z')\big),\\
\tilde{g}_{zx} &= -\frac{|\boldsymbol{q}|k_z(\boldsymbol{q})}{k_0^2}\big(1 + R'(\boldsymbol{q})\exp(2ik_z(\boldsymbol{q})z')\big),\\
\tilde{g}_{xz} &= -\frac{|\boldsymbol{q}|k_z(\boldsymbol{q})}{k_0^2}\big(1 - R'(\boldsymbol{q})\exp(2ik_z(\boldsymbol{q})z')\big),
\end{aligned}$$

all other elements of $\boldsymbol{g}$ being zero. In addition,

$$R'(\boldsymbol{q}) = \frac{k_z'(\boldsymbol{q}) - nk_z(\boldsymbol{q})}{k_z'(\boldsymbol{q}) + nk_z(\boldsymbol{q})}.$$

Bibliography

[1] E. Abbe. *Archiv f. Mikroscopische Anat.*, 9:413, 1873.

[2] Lord Rayleigh. *Phil. Mag.*, 8:261, 1879.

[3] D. Courjon, K. Sarayeddine, and M. Spajer. Scanning tunneling optical microscopy. *Opt. Comm.*, 71:23–28, 1989.

[4] C. Girard and A. Dereux. Near-field optics theories. *Rep. Prog. Phys.*, 59:657–699, 1996.

[5] J-J. Greffet and R. Carminati. Image formation in near-field optics. *Prog. Surf. Sci.*, 56:133–237, 1997.

[6] E. Synge. A suggested method for extending microscopic resolution into the ultra-microscopic region. *Phil. Mag.*, 6:356–362, 1928.

[7] E. Ash and G. Nicholls. Super-resolution aperture scanning microscope. *Nature*, 237:510–512, 1972.

[8] A. Lewis, M. Isaacson, A. Harootunian, and A. Muray. Development of a 500 Ä spatial resolution light microscope. I. Light is efficiently transmitted through $\lambda/16$ diameter apertures. *Ultramicroscopy*, 13:227–231, 1984.

[9] D. W. Pohl, W. Denk, and M. Lanz. Optical stethoscopy: Image recording with resolution $\lambda/20$. *Appl. Phys. Lett.*, 44:651–653, 1984.

[10] E. Betzig and J. K. Trautman. Near-field optics: microscopy, spectroscopy, and surface modification beyond the diffraction limit. *Science*, 257:189–195, 1992.

[11] R. Dickson, D. Norris, Y-L. Tzeng, and W. Moerner. Three-dimensional imaging of single molecules solvated in pores of poly(acrylamide) gels. *Science*, 274:966–969, 1996.

[12] N. Garcia and M. Nieto-Vesperinas. Near-field optics inverse-scattering reconstruction of reflective surfaces. *Opt. Lett.*, 18:2090–2092, 1993.

[13] N. Garcia and M. Nieto-Vesperinas. Direct solution to the inverse scattering problem for surfaces from near-field intensities without phase retrieval. *Opt. Lett.*, 20:949–951, 1995.

[14] R. Carminati and J-J. Greffet. Reconstruction of the dielctric contrast profile from near-field data. *Ultramicroscopy*, 61:11–16, 1995.

[15] R. Carminati, J-J. Greffet, N. Garcia, and M. Nieto-Vesperinas. Direct reconstruction of surfaces from near-field intensity under spatially incoherent illumination. *Opt. Lett.*, 21:501–503, 1996.

[16] J-J. Greffet, A. Sentenac, and R. Carminati. Surface profile reconstruction using near-field data. *Opt. Commun.*, 116:20–24, 1995.

[17] C. W. McCutchen. Optical systems for observing surface topography by frustrated total internal reflection and interference. *Rev. Sci. Instr.*, 35:1340–1345, 1964.

[18] P. A. Temple. Total internal reflection microscopy: a surface inspection technique. *Appl. Opt.*, 20:2656–2664, 1981.

[19] P. J. Sides and J. Lo. Measurement of linear nanometric distances between smooth plane parallel bodies by total internal reflection. *Appl. Phys. Lett.*, 69:141–142, 1996.

[20] G. E. Cragg and P. T. C. So. Standing wave total internal reflection microscopy - breaking the diffraction resolution limit. *Biophys. J.*, 78:248a, 2000.

[21] P. T. C. So, H-S. Kwon, and C. Dong. Resolution enhancement in standing-wave total internal reflection microscopy: a point-spread-function engineering approach. *Journ. Opt. Soc. Am. A*, 18:2833–2845, 2001.

[22] R. C. Reddick, R. J. Warmack, and T. L. Ferrell. New form of scanning optical microscopy. *Phys. Rev.*, B39:767–770, 1989.

[23] J. Guerra and W. Plummer. U.s. patenet no. 4681451 (1987).

[24] E. Wolf. Principles and development of diffraction tomography. In Anna Consortini, editor, *Trends in Optics*, pages 83–110. Academic Press, San Diego, 1996.

[25] P. S. Carney and J. C. Schotland. Three-dimensional total internal reflection microscopy. *Opt. Lett.*, 26:1072–1074, 2001.

[26] P. S. Carney and J. C. Schotland. Inverse scattering for near-field microscopy. *Appl. Phys. Lett.*, 77:2798–2800, 2000.

[27] P. S. Carney and J. C. Schotland. Determination of three-dimensional structure in photon scanning tunneling microscopy. *Journ. Opt. A: Pure Appl. Opt.*, 4:S140–S144, 2002.

[28] P. S. Carney, E. Wolf, and G. S. Agarwal. Statistical generalizations of the optical theorem with applications to inverse scattering. *Journ. Opt. Soc. Am. A*, 14:3366–3371, 1997.

[29] P. S. Carney, E. Wolf, and G. S. Agarwal. Diffraction tomography using power extinction measurements. *Journ. Opt. Soc. Am. A*, 16:2643–2648, 1999.

[30] P. S. Carney, V. A. Markel, and J. C. Schotland. Near-field tomography without phase retrieval. *Phys. Rev. Lett.*, 86:5874–5876, 2001.

[31] Z. Yu and S. Boseck. Scanning acoustic microscopy and its applications to material characterization. *Rev. Mod. Phys.*, 67:863–891, 1995.

[32] G. A. D. Briggs. *Acoustic Microscopy*. Clarendon, Oxford, 1992.

[33] R. A. Lemons and C. F. Quate. In W. P. Mason and R. N. Thurston, editors, *Physical Acoustics Vol. 14*, page 1. Academic, London, 1979.

[34] P. C. Clemmow. *The Plane Wave Spectrum Representation of Electromagnetic Fields*. Pergamon Press, Oxford, 1996.

[35] H. Weyl. Ausbreitung elektromagnetischer wellen über einem ebenen leiter. *Ann. Phys. (Leipzig)*, 60:481–500, 1919.

[36] P. S. Carney, J. C. Schotland, and E. Wolf. Reflection, transmission and extinction of optical power: the generalized optical theorem. *in preparation*, 2002.

[37] M. Born and E. Wolf. *Principles of Optics*. Cambridge University Press, 7th edition, 1999.

[38] E. Feenberg. The scattering of slow electrons by neutral atoms. *Phys. Rev.*, 40:40–54, 1932.

[39] H. C van de Hulst. On the attenuation of plane waves by obstacles of arbitrary size and form. *Physica*, pages 740–746, 1949.

[40] A. A. Maradudin and D. L. Mills. Scattering and absorption of electromagnetic radiation by a semi-infinite medium in the presence of surface roughness. *Phys. Rev. B*, 11:1392–1415, 1975.

[41] P. S. Carney. *Optical Theorems in Statistical Wavefields with Applications.* PhD thesis, University of Rochester, Rochester,NY, June 1999.

[42] S. I. Bozhevolnyi and B. Vohnsen. Near-field optical holography. *Phys. Rev. Lett.*, 71:3351–3355, 1996.

[43] P. Hariharan. *Optical Holography.* Cambridge University Press, 1996.

[44] D. Gabor. A new microscopic principle. *Nature*, 161:777–778, 1948.

[45] D. Gabor. Microscopy by reconstructed wavefronts. *Proc. Roy. Soc. A*, 197:454–487, 1949.

[46] P. L. Phillips, J. C. Knight, J. M. Pottage, G. Kakarantzas, and P. St J. Russel. Direct measurement of optical phase in the near field. *Appl. Phys. Lett.*, 76:541–543, 2000.

[47] E. N. Leith and J. Upatnieks. Reconstructed wavefronts and communication theory. *J. Opt. Soc. Am*, 52:1123–1130, 1962.

[48] E. N. Leith and J. Upatnieks. Wavefront reconstruction with continuous-tone objects. *J. Opt. Soc. Am*, 53:1377–1381, 1963.

[49] F. Natterer. *The Mathematics of Computerized Tomography.* Wiley, New York, 1986.

[50] C. Cohen-Tannoudji, B. Diu, and F. Laloe. *Quantum Mechanics.* Hermann, Paris, 1977.

[51] P. S. Carney, V. A. Markel, and J. C. Schotland. Near-field tomography without phase retrieval. *Phys. Rev. Lett.*, 86:5874–5876, 2001.

[52] V. A. Markel and J. C. Schotland. Inverse problem in optical diffusion tomography IV: Nonlinear inversion formulas. *Journ. Opt. Soc. Am. A*, 20: 903–912, 2003.

P. Scott Carney
University of Illinois at Urbana–Champaign
Urbana, IL 61801
United States
carney@uiuc.edu

John C. Schotland
University of Pennsylvania
Philadelphia, PA 19104
United States
schotland@seas.upenn.edu